EFFECT OF OSTEOTOMY AND PLATE ORIENTATION ON TIBIAL PLATEAU ROCK-BACK FOLLOWING TPLO USING A TIBIAL GAP MODEL

By

Edyta Bula

A THESIS

Submitted to
Michigan State University
in partial fulfillment of the requirements
for the degree of

Comparative Medicine and Integrative Biology – Master of Science

2021

ABSTRACT

EFFECT OF OSTEOTOMY AND PLATE ORIENTATION ON TIBIAL PLATEAU ROCK-BACK FOLLOWING TPLO USING A TIBIAL GAP MODEL

By

Edyta Bula

Rock-back is a recognized TPLO complication yet its cause has not been elucidated. We propose that rock-back is affected by 1) osteotomy orientation with respect to the caudal tibial cortex (uphill, normal and downhill) and 2) plate inclination with respect to the caudal tibial cortex (straight and inclined).

Tibial bone models were 3D printed from CT images of a ~25 kg dog. Models featured one of three osteotomies (uphill – 75°, normal – 90°, downhill – 105°) with a 1 mm interfragmentary gap. For each osteotomy, a 2.7 mm TPLO plate (DPS) was applied either parallel to or at a 20° angle to a best fit line of the caudal tibial cortex, representing a worse-case scenario of plate inclination. Specimens were cyclically loaded to 400 N using a custom-built loading press. Electromagnetic sensors affixed to the tibial plateau segment and distal tibial crest were used to compare tibial plateau rock-back about the mediolateral axis and roll about the craniocaudal axis.

Within each osteotomy group, rock-back was ~1.5 times greater with inclined than straight plates ($p<0.05$), which was associated with an average difference of ~1.34° ± 0.4°. Conversely, the orientation of the osteotomy had no effect on rock-back ($p>0.05$).

These findings suggest that our model can replicate rock-back, which likely results from an accentuated disruptive force couple generated by an inclined plate as compared to a plate placed parallel to the caudal tibial cortex. Standardization is recommended to align the plate parallel to the caudal tibial cortex, thus reducing the risk of rock-back.

To my mother, Halina Bula. I would not have had the ability to pursue my studies if it were not for the strength you instilled in me from a young age. Your work ethic, determination and love for others above all things continues to inspire me. I love you, always.

ACKNOWLEDGEMENTS

To my mentor and inspiration, **Dr. Loic Dejardin**. Your belief in me allowed me to achieve beyond what I imagined I was capable of. To reach for the stars and attain my highest potential. A most sincere thank you for your sacrifice, encouragement, knowledge, and guidance with my research and throughout residency. Your expertise in orthopedic surgery, engineering, biomechanical testing, and so much more is admirable. I have learned a great deal through this journey. I am honored to call you my mentor, colleague, and family and I will be forever grateful for your steadfast support.

To the members of my Masters committee:

To **Dr. Ranjan Mukherjee**, thank you for your collaboration on my research. With your guidance, I was more readily able to grasp complex engineering concepts. I am grateful for your continual support both in and out of the laboratory, as well as the laboratory space you provided to run my experiments.

To **Dr. Karen Perry**, your positive attitude and words of motivation helped me push forward when my research was difficult, and for this I am so grateful. Thank you for your support as a mentor and friend.

To **Dr. Feng Wei**, thank you for your assistance with evolving this project into what it has become. Your expertise in biomechanical testing is unparalleled.

To **Dr. Michael Lavagnino**, I am very grateful for your support and collaboration throughout this project. Thank you for your assistance when this project was at its infancy.

I would like to also thank **Dr. Mahmoud Abdullatif** and **Dr. William Chung** for their unwavering friendship and assistance during the experimental phase of this project. Particularly Dr. Abdullatif for the time dedicated to running the experimental phase of this research and Dr. Chung for his expertise in design of the custom-built loading press.

Thank you to **Sichao Wang** for assistance with determining the appropriate statistical analysis and training in statistical software.

Finally, I would like to acknowledge and thank **DePuy-Synthes** for their implant donation and support throughout this project. I look forward to future collaboration.

This work was supported by the **Michigan State University Endowed Research Funds** through the **Comparative Medicine and Integrative Biology Department**.

PREFACE

Being born and raised in Detroit, Michigan, I knew I wanted to become a veterinarian from a young age, as is the fantasy of many children. It was not until later in life that I realized animals were my muse and my refuge from the bad going on around me. I always wanted to be a voice for the voiceless – a voice for the innocent. Through veterinary school, I became inspired to pursue specialized training in small animal surgery with a dual-program residency and masters. Paired with academic research specifically tailored to orthopedics and engineering, I became drawn to the world of joint biomechanics. This thesis is a collection of my work with a diverse and collaborative team of researchers, engineers, and scientists. I focus on improving the surgical outcome of dogs with the most common joint disease present in orthopedics, that of the cranial (anterior) cruciate ligament. Through 3D design and modeling, 3D printing, and standardization of biomechanical testing using electromagnetic tracking software, I hope to inspire and develop a deeper understanding of the canine stifle following TPLO. Subsequently, standardization of TPLO osteotomy technique and implant placement will enhance future resident training and improve patient outcomes.

TABLE OF CONTENTS

LIST OF TABLES

LIST OF FIGURES

KEY TO ABBREVIATIONS

TPLO	Tibial Plateau Leveling Osteotomy
CrCL	Cranial Cruciate Ligament
CaCL	Caudal Cruciate Ligament
TPA	Tibial Plateau Angle
TPS	Tibial Plateau Slope
CrTT	Cranial Tibial Thrust
3D	3 Dimensional
CAD	Computer-Aided Design
OCS	Object Coordinate System
CS	Coordinate System
CT	Computed Tomography
STL	Stereolithography
IPA	Isopropyl Alcohol
DPS	DePuy-Synthes
OTS	Optical Tracking System
EMTS	Electromagnetic Tracking System
EMS	Electromagnetic Sensors
NDI	Northern Digital Inc
DoF	Degrees of Freedom
N	Newton
Nm	Newton-Meters

MPa	Mega Pascal
Hz	Hertz
Kg	Kilogram
µm	Micrometer
µ	Micron
mm	Millimeter
mm/sec	Millimeter per second
C	Celsius
F	Force
MA	Moment Arm
d	Distance
min	Minutes
OD	Outer Diameter
ID	Inner Diameter
CTC	Caudal Tibial Cortex
ANOVA	Analysis of Variance
BW	Body Weight
BCS	Body Condition Score
DI	Downhill Inclined
DS	Downhill Straight
UI	Uphill Inclined
US	Uphill Straight
NI	Normal Inclined

NS	Normal Straight

CHAPTER 1

DESIGN OF A 3-DIMENSIONAL TIBIAL GAP MODEL

Introduction

Traditionally, cadaveric specimens have been used in biomechanical testing of veterinary bone models for assessment of implant strength, failure mode, or failure load during compression loading. Kowaleski et al found that Synthes TPLO plates were stiffer when loaded in compression compared to Slocum TPLO plates using a cadaveric gap model[1]. More recently, 3D models have gained popularity in veterinary medicine for surgical guide design (patient-specific instrumentation) and rehearsing surgical procedures pre-operatively or for training purposes[2,3,4]. There is a paucity of information regarding 3D printing for biomechanical testing of bone specimens in veterinary medicine. Marturello et al found that machined short-fiber epoxy acts as a surrogate to the native feline femur with regard to torsional compliance, angular deformation, and torque to failure[5]. However, in this same study, 3D printed bone models (resin or plastic-based) exhibited excessive torsional compliance and plastic deformation compared to machined samples and native femurs.

Although 3D models lack the exact composition of native bone, standardization and reproducibility of prints provides consistency during experimental testing and eliminates the inherent variability of cadaveric specimens. Thus, 3D printed models act as their own control in an experimental setting. In addition, 3D printing is efficient, reliable, and may save costs associated with acquiring cadaveric specimens. On the contrary, cadaveric bone varies in bone density, bone size and may incorporate underlying diseases that alter bone density such as hyperadrenocorticism, casting doubt on the accuracy of data acquired.

The aim of this phase of research was to design a consistent 3D tibial model from an average-sized (~25 kg) dog with no underlying orthopedic disease. The CT scan of this dog was processed in 3D software prior to export to the design module.

Materials and Methods

Hospital records from Michigan State University were searched to find a CT of a tibia from a mid-sized dog (BW ~25 kg, BCS 7/9) without evidence of stifle osteoarthritis and for which standard bilateral TPLO radiographs had been taken. The right stifle was selected for 3D segmentation and modeling. The TPA of the right stifle was measured on Orthopedic planning software (Materialise Orthoview) and was found to be 32°.

The CT was imported into 3D software and the right tibia isolated using segmentation (Materialise Mimics). The cortical width of the tibia was rendered from the CT and the medullary cavity was hollowed to replicate *in vivo* bone densities. The tibia was then exported into a design module (Materialise 3-Matic). Anatomical and mechanical axes were established to ensure accuracy during subsequent design. These included sagittal, transverse, coronal and mechanical tibial axes (**Figure 1.1**)

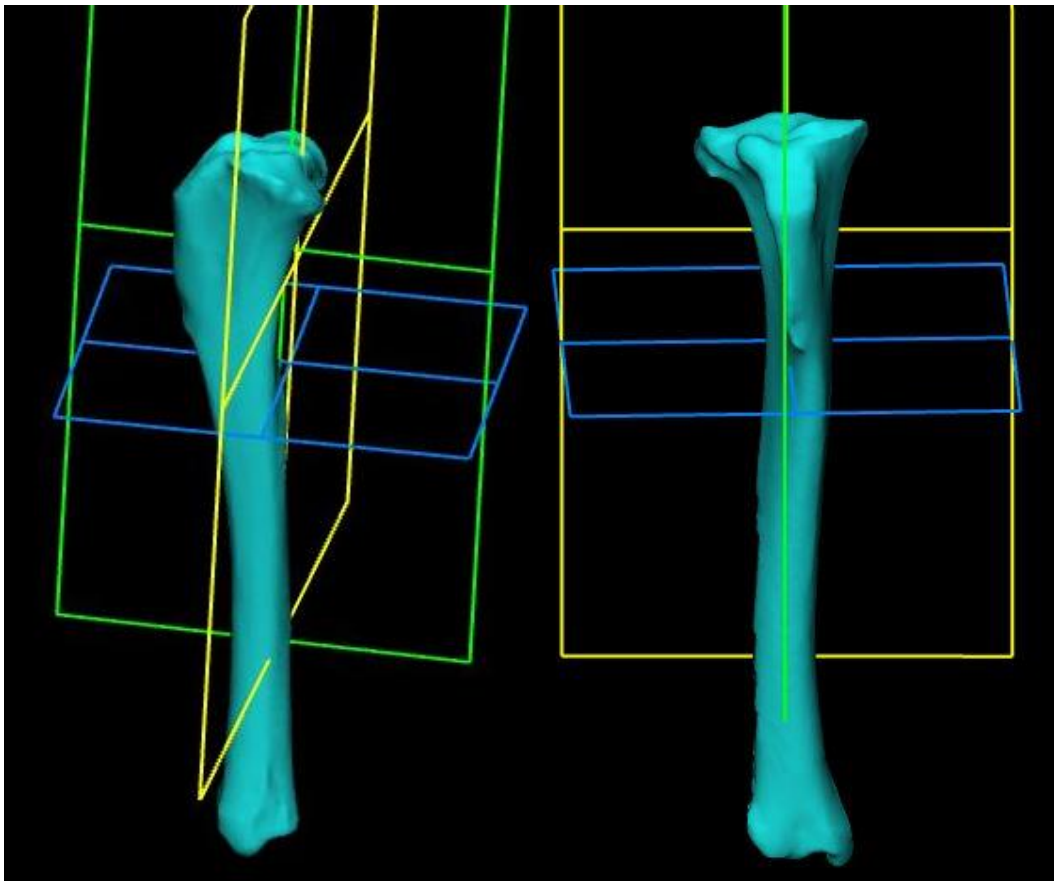

Figure 1.1. Design of anatomical tibial planes post segmentation based on CT landmarks

Following identification of the sagittal plane (*green*), an additional orthogonal plane that included the tibial mechanical axis was created (yellow). The last plane (blue) was orthogonal to both the sagittal plane and the plane passing through the tibial mechanical axis. **Left** – orientation of the tibia with the medial cortex closest to the reader. **Right** – tibia rotated 90° counterclockwise to reveal its cranial orientation.

The tibia was trimmed at its mid-diaphysis. A spherical depression was designed along the tibial plateau centered between the tibial tubercles. The diameter of the sphere (19.05 mm) was equivalent to the brass ball used during compression loading. The spherical depression was placed at a tibial plateau depth of approximately 50% of its diameter to ensure appropriate seating of the brass ball without slippage (**Figure 1.2**).

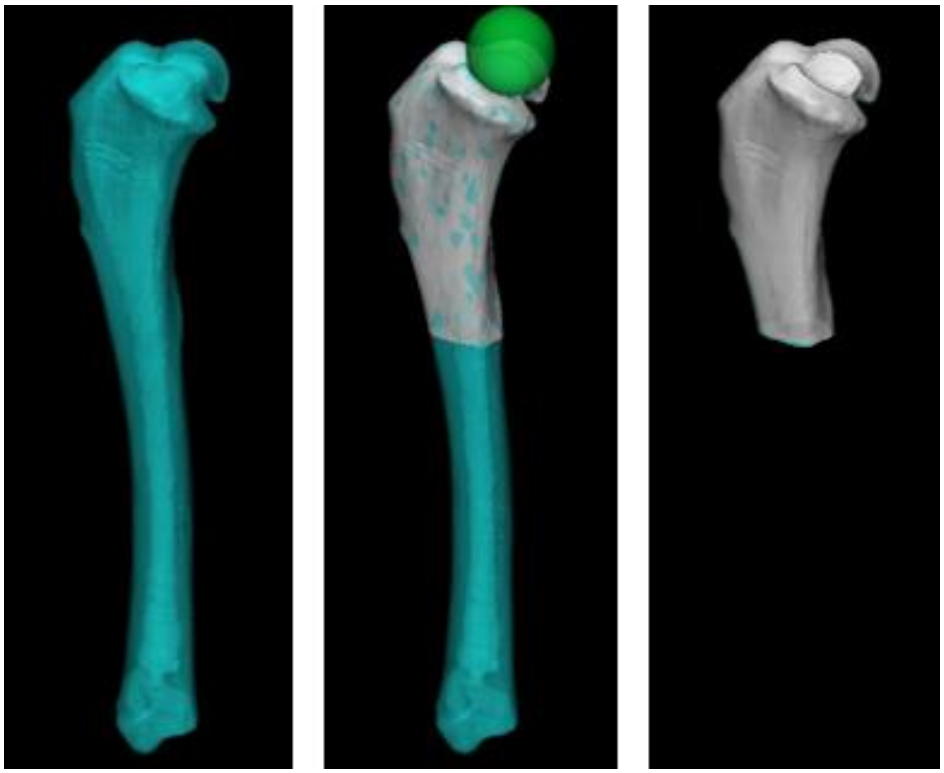

Figure 1.2. Design of tibial spherical depression

Segmented tibia (**left**) with design of a spherical depression centered on the tibial tubercles (**center**). The spherical diameter is 19.05 mm to couple with the loading sphere. The final depression is based on a spherical recession of 50% of its diameter and the tibia is trimmed at its proximal diaphysis (**right**).

A cylindrical base was designed at the distal end of the trimmed tibia to accept the fixed loading base of a custom-designed table press. The cylindrical base was designed to be continuous with the tibial shaft approximately 1 cm beyond the distal aspect of the plate using a fillet technique. This base contained an inner hollowed cylinder to permit drainage of support material post-printing. In addition, a radial cranial notch was designed to lock into the base fixture of the custom-built loading press to eliminate rotational forces of the model (**Figure 1.3**).

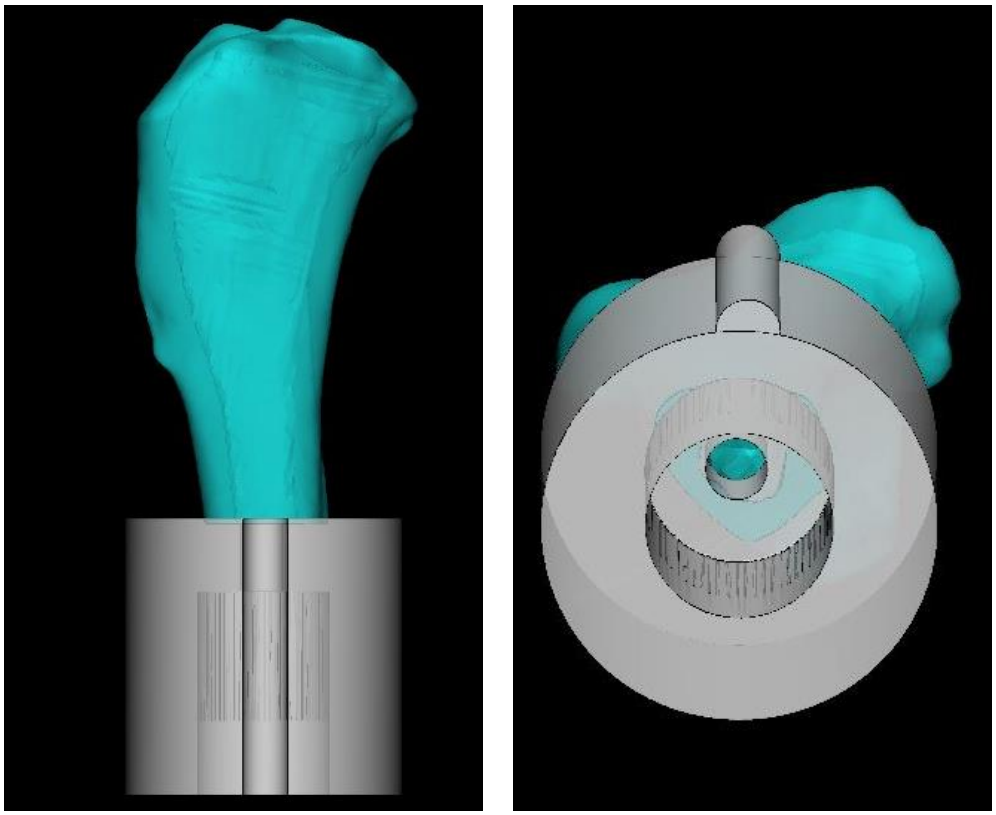

Figure 1.3. Depiction of the distal loading cylinder merged with the cut tibia to create a single specimen

Design of the loading cylinder includes a hollowed center with a draining hole to allow drainage of the support material from the medullary canal. A radial extrusion on the medial face of the construct is created to counteract rotational forces when coupled to the loading base of the press.

Following the creation of coupling fixtures, three osteotomies were designed (uphill, normal, downhill) in relation to the caudal tibial cortex (**Figure 1.4**). A best-fit line was digitally created approximating the caudal tibial cortex. The osteotomy radii were 21, 24, and 27 mm for uphill, normal and downhill osteotomies respectively. Uphill, normal and downhill angles, measured on the distal tibial segment, were 75°, 90° and 105° respectively, in relation to the best fit line of the caudal tibial cortex. The cranial aspect of all osteotomies was centered at the midpoint between the cranial footprint of the CrCL and caudal footprint of the patellar ligament on the tibial tuberosity. After creation of all osteotomies, the model was digitally segmented into its two respective parts (i.e., tibial plateau segment and distal tibial segment).

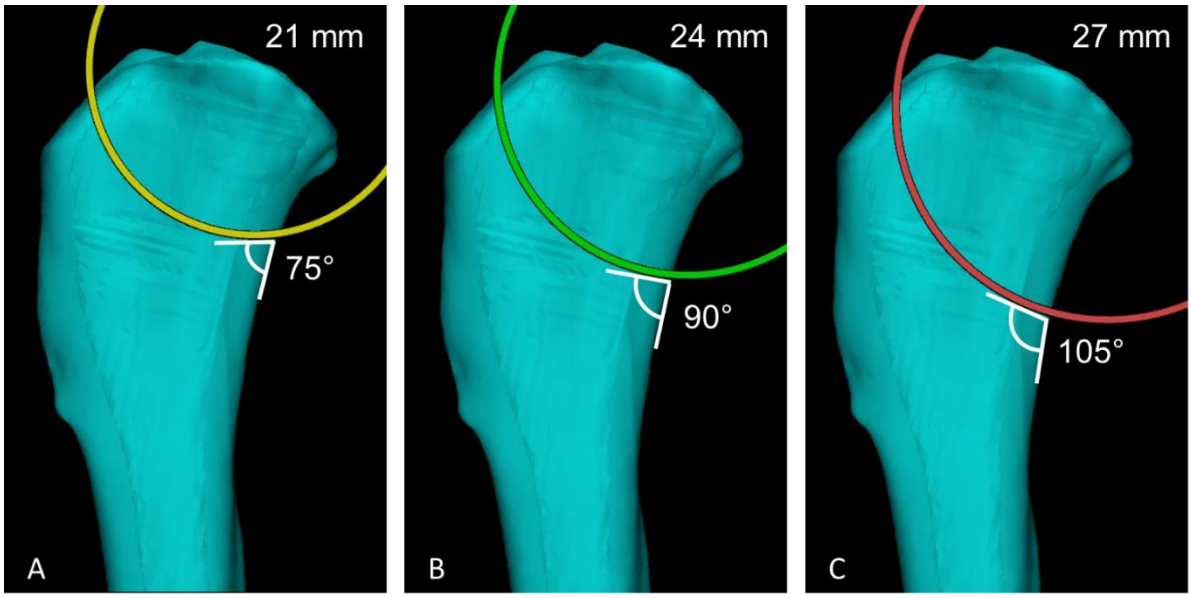

Figure 1.4. Depiction of the three osteotomies designed for the final phase of experimental testing

All osteotomies are designed in relation to the caudal tibial cortex. The cranial point of each osteotomy is placed at the midpoint between the tibial tuberosity and footprint of the cranial cruciate ligament on the tibial plateau. Radii of 21, 24, and 27 mm were created for uphill, normal, and downhill osteotomies respectively. The uphill osteotomy has an acute exit angle of 75° (**A**), the normal osteotomy 90° (**B**) and the downhill osteotomy an obtuse angle of 105° (**C**). Next, the proximal tibial segment of each model was digitally rotated to a final TPA of 5° based on an initial TPA of 32° (total rotation of 27°) (**Figure 1.5**). A 1 mm gap was created between segments by translating the tibial plateau segment along its inertia axis to maintain an even gap width. This small gap represented a TPLO clinical case scenario whereby complete fragment compression may not be achieved intra-operatively.

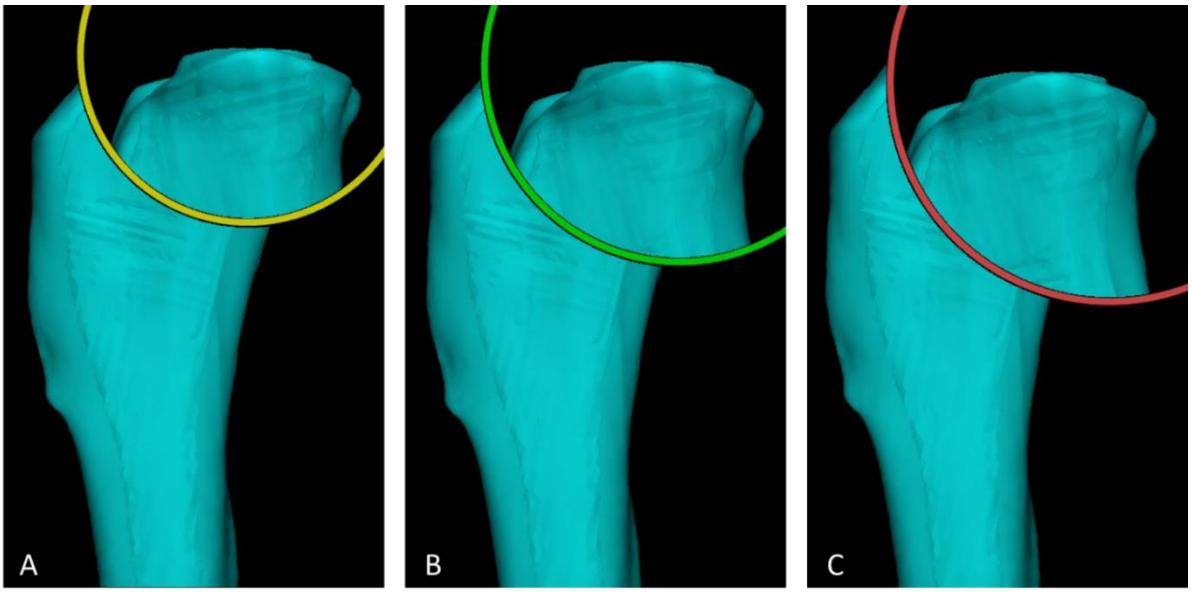

Figure 1.5. Digital rotation of the tibial plateau segment for each respective osteotomy

A final TPA of 5° is achieved as recommended for TPLO. **A** – uphill osteotomy. **B** – normal osteotomy. **C** – downhill osteotomy.

The STL of a 2.7 mm TPLO plate provided by DPS was imported and translated to overlay the medial tibia as would be performed during an *in vivo* TPLO procedure. The plate was placed either straight (0°) or inclined (20°) in relation to the caudal tibial cortex best fit line (**Figures 1.6 and 1.7**). Plate inclination was achieved by rotating the plate the desired amount about the craniocaudal or y-axis. A 20° incline was chosen to represent a worst-case scenario outside of manufacturer recommended guidelines of plate placement where a small level of incline in the order of magnitude of ~8-10° with respect to the tibial mechanical axis (rather than caudal cortex) is deemed acceptable.

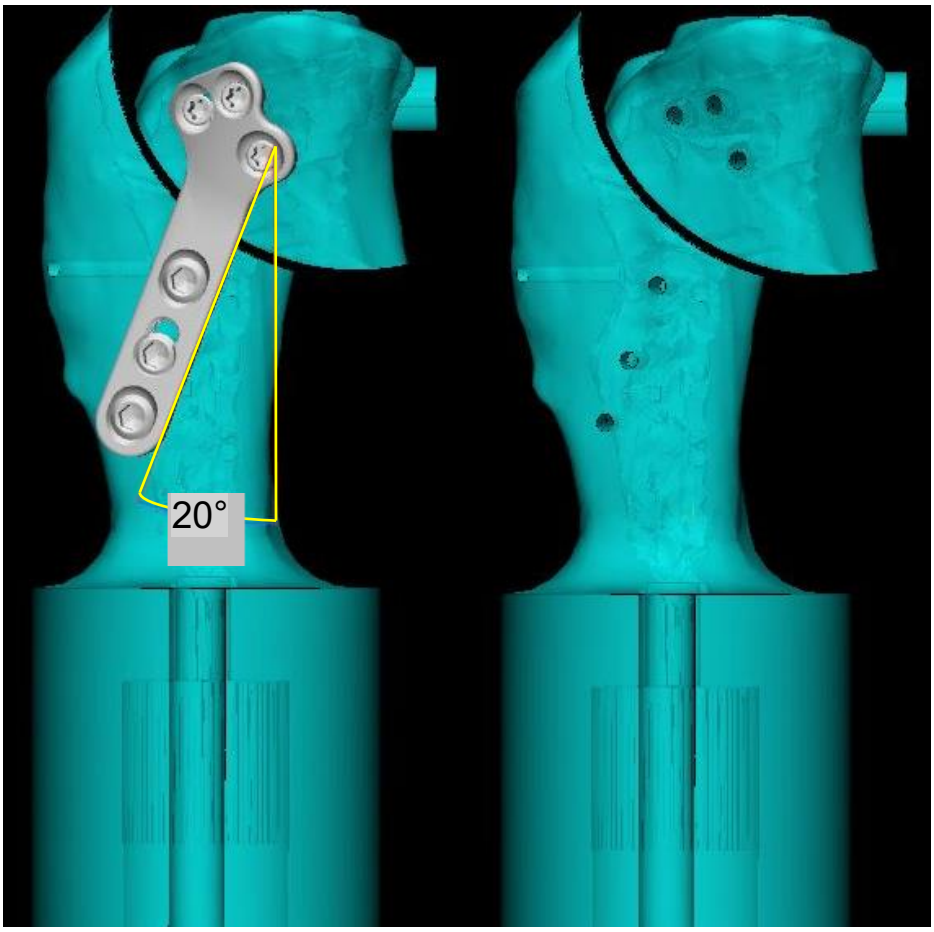

Figure 1.6. Overlay of an inclined TPLO bone plate STL file to design pilot holes

Left – A downhill osteotomy with a 2.7mm TPLO bone plate placed flush along the medial cortex at a 20° incline from the caudal tibial cortex is shown. 2 mm pilot holes are designed to follow the trajectory of locking screws in the proximal plate and cortical screws in the distal plate segment. The tibial plateau segment has been translated 1 mm from the distal tibial segment along the inertia axis. **Right** – the same model following pilot hole design.

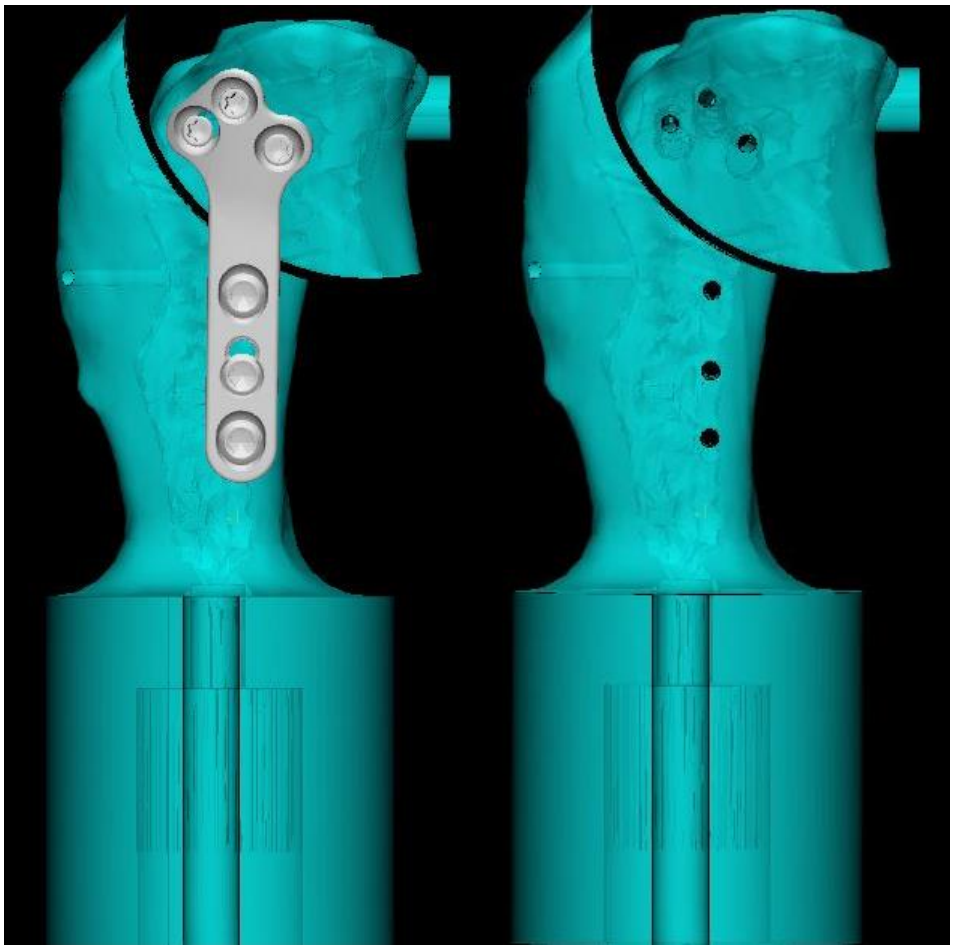

Figure 1.7. Design of pilot holes for a plate oriented parallel to the caudal tibial cortex with the TPLO STL overlay

Left – A downhill osteotomy with a 2.7mm TPLO bone plate placed flush along the medial cortex parallel to the caudal tibial cortex is shown. 2 mm pilot holes are designed to follow the trajectory of locking screws in the proximal plate and cortical screws in the distal plate segment as was done for the inclined model. **Right** – the same model following pilot hole design, showing parallel plate placement to the caudal tibial cortex.

Following accurate plate placement, screw pilot holes were designed by following the trajectory of the digital plate screws, creating hole diameters of 2.0 mm to accept both cortical and locking screws. The distal tibial segment contained all cortical screws placed in neutralization mode to maintain the 1 mm gap between segments. The tibial plateau segment accepted all locking head screws. For the tibial plateau segment, guides were designed within the hollow medullary cavity to direct screw placement post-printing as these screws converge on the trans-cortex. These guides were designed with an outer diameter of 4 mm and an inner diameter of 2.7 mm and were fused to the inner tibial cortex to ensure the cortical pilot hole remained at 2 mm in diameter. The cortical pilot holes did not require guides as they were easily placed with a straight trajectory.

Two additional pilot holes were created on each tibial segment to accept electromagnetic sensors (**Figure 1.8**). These were designed by subtracting cylinders of a 1.8 mm diameter to accept the sensors and restrict movement within the pilot hole. The first hole was placed on the cranial aspect of the distal tibial crest, oriented parallel to the sagittal plane. The depth of this hole extended through the entirety of the cortex. The second pilot hole was placed within a cylinder designed to extend from the caudal tibial plateau. This hole was centered between the medial and caudal protuberances of the caudal tibial plateau. The depth of this pilot hole was 5 mm.

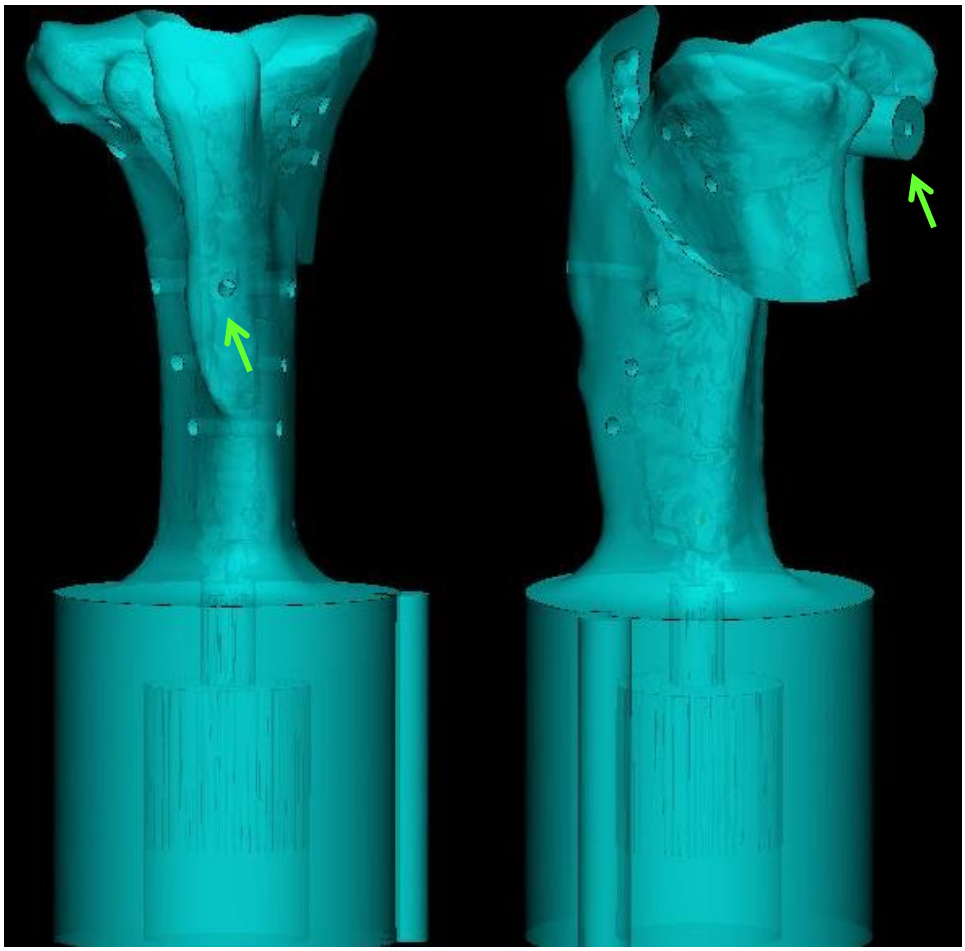

Figure 1.8. Guide hole design for electromagnetic sensors

Two pilot holes were designed at 1.8 mm diameter to accept an electromagnetic sensor in the proximal and distal tibial segments. **Left** – sensor 1, placed in the distal tibial segment, is located at the level of the distal tibial crest and is parallel to the sagittal plane (*green arrow*). **Right** – sensor 2 is placed in the tibial plateau segment also parallel to the sagittal plane (*green arrow*). Note the cylindrical extension designed to allow visualization of this sensor within the caudal plateau during testing.

A total of six models were created, each consisting of one plate configuration (straight or inclined) and one osteotomy orientation (uphill, normal, downhill). Thus, the six groups were as follows: downhill inclined (DI), downhill straight (DS), normal inclined (NI), normal straight (NS), uphill inclined (UI) and uphill straight (US).

Subsequently, a model-specific cast was constructed in the same 3D software to maintain a 1 mm osteotomy gap during post-printing placement of the bone plate (**Figures 1.9 and 1.10**). To achieve this, the medullary canal of each respective tibial segment was removed, and all holes closed to ensure successful subtraction of the model from its cast. A block was then designed to match the lateral cortical profile of each completed tibia. A negative imprint of the lateral aspect of each tibia was created by subtracting the contour of the tibial cortex from the block. A 1 mm ledge was maintained within the imprint retaining the interfragmentary gap. The screw holes designed on each model were extended into the cast as 5 mm diameter holes to accept both cortical and locking screws. The larger diameter of these screw holes prevented engagement of the screw threads when affixing the plate post-printing, thus allowing feasible uncoupling of the model from its cast. A separate cast was designed for the cylindrical base of all models in a similar fashion. The model-specific casts were trimmed along their edges to ensure a press-fit of each printed model without difficult uncoupling. This required several trial runs of design and printing prior to finalization of each model-specific cast.

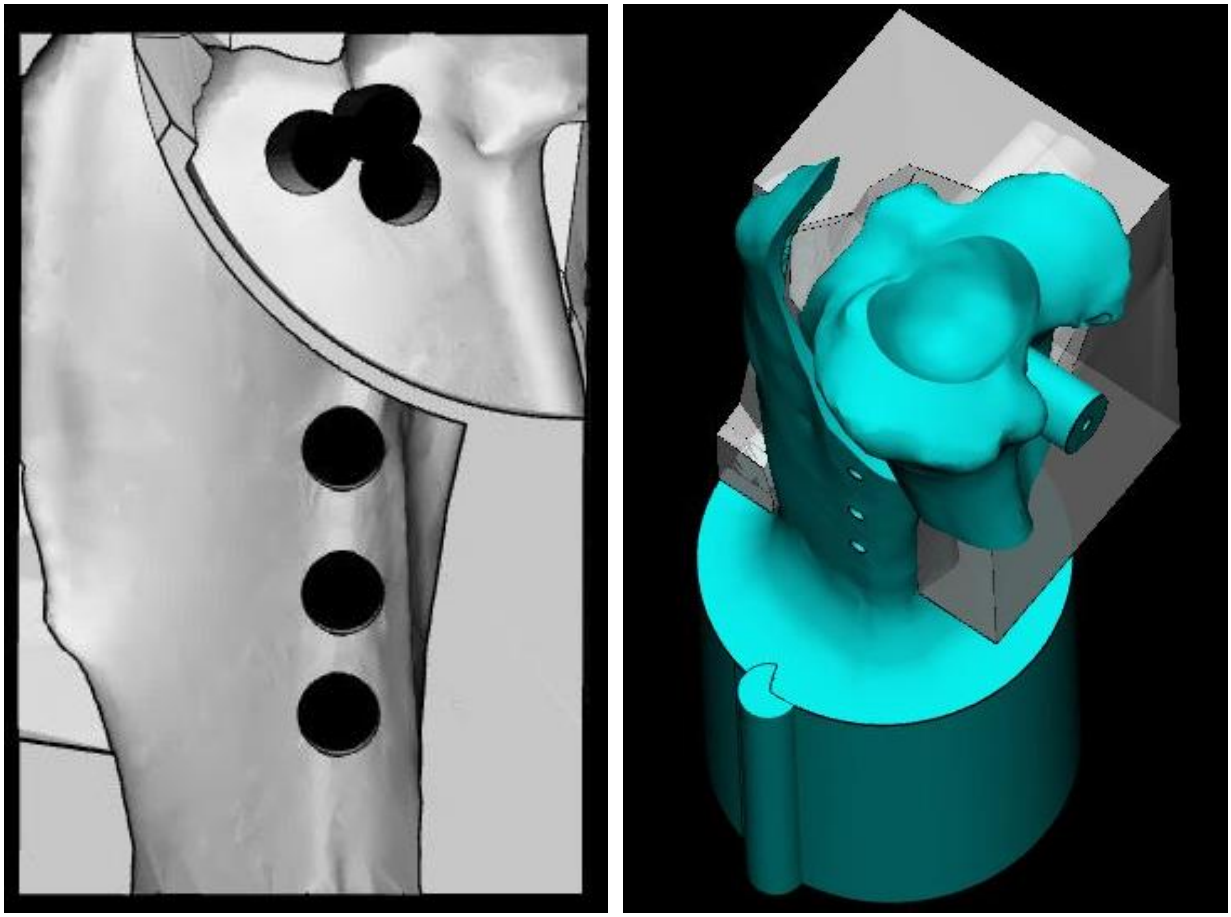

Figure 1.9. Illustration of a model-specific cast designed for a specimen with a downhill osteotomy and straight plate inclination

Pilot holes within the cast are 5 mm in diameter to allow ease of removal after plate placement (**left**). The model fits into its respective cast as a press-fit system (**right**).

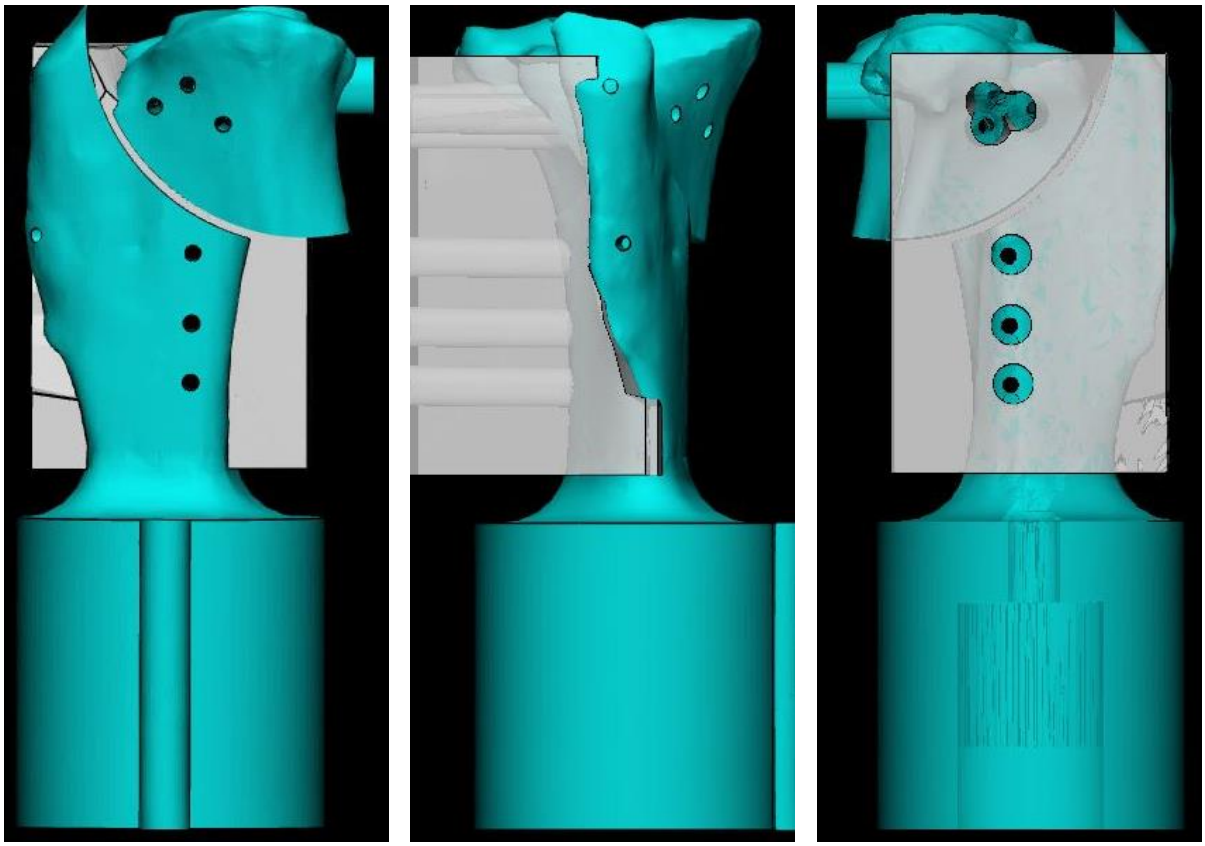

Figure 1.10. Model-specific cast shown from three perspectives

Left – the medial surface of the bone is shown. **Center** – cranial perspective. **Right** – the lateral aspect of the tibia is shown secured into the cast. Notice how the path of the model screw holes follow that of the cast pilot holes.

All six models in addition to their dedicated casts and one cylindrical base cast were uploaded as STL files to a resin-based 3D printer (Formlabs Form2). Based on its material properties and feasibility of implant placement on the models, standard white resin material was selected. Standard resins have high resolution (25 μ) and tensile strength. The ultimate tensile strength of standard white resin post-cure is 65 MPa, permitting implant and load application without a high risk of model failure in the form of breakage (Material Data Sheet Formlabs). Each model was printed as two separate parts, the proximal tibial segment and the distal tibial segment with its attached base. The casts were printed using tough resin material, which provides both strength and compliance. Compared to standard resin, tough resin has an ultimate tensile strength of 55.7 MPa post-cure with a capability to elongate at 24% compared to standard resin at 6.2% (Material Data Sheet Formlabs). Compliance of the tough resin enabled a press-fit system between each cast and model without resin breakage. All models and casts were printed using preform software (Formlabs) with a layer thickness of 100 μm and support resin connecting the part to the platform. Following the completion of each print, a power wash cycle (Form Wash) using IPA was used on each part to remove uncured resin. Standard resin underwent a 10-minute power wash cycle whereas tough resin a 10-minute power wash cycle followed by a 10-minute soak in stagnant IPA. Next, supports were removed manually, and parts placed in the cure machine (Form Cure). Standard white resin was cured for 30 min at 60°C and tough resin for 60 minutes at 60°C according to manufacturer guidelines.

Following the printing and curing process, each model was engaged into its respective cast and standard TPLO instrumentation was used to affix a 2.7 mm TPLO

plate onto each model, maintaining a 1 mm gap osteotomy. Three locking screws were placed in the proximal segment and three cortical screws in the distal segment. All screws extended 3 threads beyond the trans-cortex and were secured at uniform torques by means of a calibrated screwdriver (1.50 Nm locking and 0.6 Nm cortical, respectively). These torques were based on the TPLO surgical technique guide (DPS) where a 0.8 Nm torque is used for the 2.7 locking screws. We elected to increase this torque to 1.5 Nm to ensure complete coupling. The 0.6 Nm torque for cortical screws was chosen after pilot models fissured at the model-implant interface due to excessive compression of the plate against the bone at the recommended 0.8 Nm of torque. By decreasing the torque to 0.6 Nm for cortical screws, none of the subsequent models broke.

Results

Initial printing of models was performed using Polyjet technology with a resin-based photopolymer printer (*Connex Objet 350, Stratasys*). Material used was VeroWhite resin. Although prints withstood drilling during TPLO bone plate placement without any failure, this print material was not cost-efficient. Consequently, Standard White resin (*FormLabs2*) was utilized for any subsequent prints.

With early pilot models, no pilot holes were designed for TPLO bone plate placement prior to 3D printing. This proved difficult due to lack of consistency of bone plate placement on each model. In addition, drilling directly into the dense 3D print material without a specified pilot hole induced fissures into the bone replica. Therefore, the STL file of a 2.7 mm right-sided TPLO bone plate (DPS) with screws trajectories was overlaid in the design module and pilot holes created for successive specimens. Bone plate placement following pilot hole design was feasible, accurate and did not induce any cracks or propagating fissures into any of the specimens utilized for testing.

Early 3D printed models contained a uniform bone density with no differentiation between cortical and medullary bone. With this method, both printing time and cost of 3D printing were increased as more resin was utilized. Drilling through a solid specimen was challenging and deemed unrealistic as it poorly replicated the structure of the native tibia. Thus, segmentation of models was altered to more precisely mimic native bone by hollowing the medullary cavity and retaining the same width of cortical bone as defined by the CT.

Final test models were printed with no complication and in a standardized manner. No fissure or failure was noted during placement of the bone plate onto the specimens and drilling was feasible and efficient.

Discussion

This phase of research involved the use of 3D printed bone models to represent a TPLO gap model. A tibial gap model for TPLO testing when comparing implant stiffness has been previously utilized in the veterinary literature successfully using cadaveric specimens[1]. However, limitations with cadaveric specimens exist such as difficulty with acquisition, labor costs, inherent differences of bone characteristics between specimens, time required for dissection and isolation of the bone of interest and storage considerations.

On the other hand, the use of 3D printed bone models eliminates these concerns as standardization is inherent to 3D printing once a model has been designed. This model may be stored for prolonged periods without degradation; however, consideration must be given to properly storing prints away from UV light as this causes brittleness over time. It is important to consider the costs of purchasing and maintaining a 3D printer, resin supply, and awareness of and proper handling of 3D prints during the printing, washing, and curing processes. However, familiarization of these practices is feasible and not technically demanding. Another limitation to 3D prints is their inability to replicate the exact properties of native bone as they do not account for the anisotropy and inhomogeneity of native bone. Thus, 3D printed models may not be appropriate in all settings of biomechanical testing. In our research, the goal was to replicate a TPLO bone model to compare differences in technique; as such, analyzing failure modes/load or bone properties was not assessed.

Using 3D prints for biomechanical testing is reliable as each model acts as its own control. This research utilized the CT of a single canine with no underlying orthopedic

conditions of the leg of interest, to reduce inter specimen variation and improve standardization. The bone plate STL file was the same size and design for every model (DPS), further ensuring consistency. A previous study evaluating rock-back did not show a difference in magnitude of rock-back when evaluating patient weight or implant type[6]. Thus, we chose a patient with an average body weight and size and a TPLO plate that was appropriate for the size of bone. In addition, it was feasible to make adjustments to the models throughout this project without loss of data or having to completely redesign specimens. Therefore, by use of consistent 3D prints, this research project was able to focus on specific rock-back factors without the limitations inherent to cadaveric specimens.

APPENDIX

Standard Operating Procedure for Design of 3D Bone Models

1. **Export CT to Materialise**
    a. PACS → Export → DICOM
2. **Materialise Mimics Segmentation**
    a. Threshold 300-2000 (CT bone – custom)
    b. Crop mask → isolation of tibia/fibula/tarsus
    c. Split mask segmentation → isolation of tibia
    d. Smoothen
3. **Export Segmentation to 3-Matic**
    a. File → export → MDCK file
    b. All units = mm
4. **Anatomical Plane Design**
    a. Analyze → create line → fit inertia axes
        i. Fitting method = based on mesh
        ii. Fitting entity = bone
    b. Update OCS to CS
        i. Entity = tibia
        ii. Method = inertia axis
    c. **Mechanical Axis:**
        i. Create analytical sphere → center and radius
            1. CenterPoint = (-37, -98.3191, 155.6997)
            2. Radius = 9.5
            3. Tolerance = 0.01

ii. Create 2 eminence points

1. Coordinate 1: (-45.1607, -123.1601, 330.7884)
2. Coordinate 2: (-50.6275, -121.2184, 330.2893)

iii. Connect line between two eminence points (length = 5.8228)

1. Create midpoint coordinates: (-47.8941, -122.1893, 330.5389)

iv. Datum plane = through 2 points, perpendicular to view

1. Point 1 = center of tibial tubercles
2. Point 2 = center of talus

d. **Caudal Axis:**

i. Create two points

1. Coordinate 1: (-60.5424, -115.2160, 319.6284)
2. Coordinate 2: (-40.1201, -114.8148, 323.4057)

ii. Create line connecting the two points

1. Create midpoint coordinates: (-50.3313, -115.0154, 321.5171)

iii. Create new datum plane → through 1 point, parallel to a plane

1. Point = midpoint (of caudal points)
2. Plane = mechanical axis datum plane

iv. Can now interactively rotate this to either align about the two points

1. Or “align”
    a. Fixed entity = datum plane (mechanical axis)
    b. Moving entity = datum plane (caudal axis)
    c. “Apply” → new screen
    d. Entity on fixed part = datum plane

e. Entity on moving part = datum plane

f. Align operation = parallel

e. **Transverse Axis:**

i. Normal and origin to mechanical axis

1. Normal = mechanical axis line

2. Origin = center of tibial tubercles point

f. **Sagittal Axis:**

i. 90° to the caudal axis

ii. Create datum plane

1. Origin = center of tibial tubercles

2. Parallel plane = caudal axis

iii. Align → rotate/translate → main entity = sagittal plane (new plane just created)

1. Transformation = rotate

2. Enable snapping at angle step = 90° (perpendicular to caudal axis)

5. <u>Loading Cylinder</u>

a. Trimming tibia

i. Finish → trim → remove inner → draw box → apply

b. Design → creative primitive → create cylinder

i. Diameter = 38.1 (19.05 radius)

ii. Length = 38.1

c. Hollow → inside thickness 10

i. Inside hollow hole = 18.1

d. Second cylinder (18.1 diameter) → subtract from main cylinder

i. Note: leave thickness static at top

e. Third cylinder (draining hole) → diameter = 6

i. Subtract from loading cylinder

f. Cranial notch = cylinder with radius = 3

g. Meniscal support = fillet

i. Thicken distal tibia with push/pull feature

ii. Boolean union distal tibia with cylindrical base

iii. Fillet → distal tibial curve to loading cylinder face

1. Radius = 8

6. <u>Spherical Depression</u>

Perform before osteotomy (otherwise boolean subtraction will not work)

a. Design → create primitive → sphere

i. “center and radius”

1. Center = eminence center point

2. Radius = 9.525

ii. Interactively translate sphere as needed

b. ***Dimensions***: 19.05, sink to 50%

c. Create analytical point at cranial aspect of medial tibial eminence

i. Point coordinates: (-41.4996, -134.2739, 330.8750)

d. Create second analytical point at caudal tibial cortex off medial tibial plateau

i. Point coordinates: (-37.2925, -114.0097, 322.7500)

e. Find midpoint and create third analytical point
    i. Midpoint coordinates: (-39.39605, -124.1418, 326.8125)
    ii. Center of sphere is midpoint → translate along x-axis (based on the tibial eminence center point (-47.8941)
    iii. Center of rotation of tibial plateau
f. Thicker depression:
    i. Design → loft → type = surface loft
        1. Entity 1 = bad contour line 1
        2. Entity 2 = bad contour line 2
        3. Method = smooth
        4. Direction = orthogonal
        5. Detail = 1
        6. Click “merge” and “remove original”
    ii. Alternate option: design → extrude → depth 2 extrusion (2 mm)
        1. Separate part → separate shells to parts
        2. Remove unnecessary loft parts (free floating)
        3. Boolean union main segment, loft, and extrusion
g. Alternate thicker depression:
    i. Finish → push/pull
        1. Ctrl = pull (use pull primarily)
        2. Shift = push
        3. Ctrl + roll = diameter adjustment
    ii. Wall thickness analysis

1. Analyze → measure analysis locally to determine proper thickness

7. <u>Osteotomy</u>

a. CTC “best fit line”:
    i. Analyze → create line → method = datum plane intersection
        1. Plane 1 = sagittal axis
        2. Plane 2 = mechanical axis
    ii. Translate to align with CTC (translation in y-axis)
b. Create sketch off sagittal axis
c. Center coordinate for each saw blade circle in sketcher
d. ***Normal osteotomy***
    i. Radius = 24
    ii. Saw center: (-47.7332, -122.2003, 327.6364)
        1. D1 = 10.54; D2 = 10.14
    iii. Angle = 90°
e. ***Uphill osteotomy***
    i. Radius = 21
    ii. Saw center: (-48.2853, -125.9889, 328.3874)
        1. D1 = 11.05; D2 = 9.67
    iii. Angle = 75°
f. ***Downhill osteotomy***
    i. Radius = 27
    ii. Saw center: (-47.7537, -117.8774, 325.9743)

1. D1 = 10.54; D2 = 11.92

iii. Angle = 105°

g. Alternative: create circle over 3D model

i. Import each circle into respective sketch

ii. Select geometry → click on circle to highlight → right click on circle → convert to sketch curves → creates your center point

iii. Create circle → snap to center point and overlay on your curve

iv. Analyze → create point → snap to your sketch center point

v. Sketch to part

1. Right click on sketch in object tree → export sketch

h. Duplicate sketch (retain original copy)

i. Offset width

1. If using “offset”, need to perform twice (1 external, 1 internal)

2. If using “offset width”, need to input 2 and it offsets it in either direction equally

3. Click “remove original” for proper extrusion

ii. Design → extrude → entities = sketch

1. Parameters = solid

iii. Finish → trim → entities = extrusion

1. Parameters = remove inner

2. Create radial osteotomy

3. Duplicate part

iv. Design → cut

1. Entities = whole tibia
2. Cutting entity = extrude

8. <u>Tibial Plateau Rotation</u>

a. Mark → shell → mark tibial plateau segment → right click “marked triangles” in object tree → separate → copy to part → new part
b. Mark distal tibia in separate shell/new part
c. Do not rotate with gap segment
d. Align → rotate
    i. Entities = tibial plateau segment
    ii. Rotation parameters:
        1. Method = around axes
            a. Angle = 27° (initial TPA 32°)
                i. Final TPA: 5°
            b. Around x-axis (all others remain at 0)
        2. Rotation origin = midpoint of sphere/rotation
            a. Downhill: (-47.7537, -117.8774, 325.9743)
            b. Normal: (-47.7332, -122.2003, 327.6364)
            c. Uphill: (-48.2853, -125.9889, 328.3874)

9. <u>Screw Holes (2.7 mm DPS Plate)</u>

a. Align bone plate with medial tibia:
    i. N-point registration
        1. Select bone, plate, bone, plate (alternate)
    ii. Global registration (after N-point registration)

iii. Keyboard shortcut: F3

b. Create primitive cylinder via two-point method
    i. Center point on head of screw, second center point on screw tail
    ii. Shading mode = filled with triangle edges to identify center
    iii. Boolean subtract each cylinder from model
c. Straight plate: align with CTC (line previously designed)
d. Inclined plate:
    i. Rotate straight plate 20°
    ii. Align → rotate → entity = plate
        1. Method = around axis
        2. Angle = -20 (x-axis)
        3. Rotation origin = center point of most proximal screw hole
e. 2.7 TPLO plate drill holes:
    i. Locking = 2.0mm drill bit
    ii. Cortical = 2.0mm drill bit
f. Proximal segment medullary guides for screw placement
    i. Inner diameter = 2.7
    ii. Outer diameter = 4
g. Boolean subtract inner from outer for medullary guides
h. Boolean union medullary guide to tibial plateau segment
i. Trim tool → trim guides to be flush with tibial plateau segment
j. To split portions of your plate/screws for ease of cylinder design:
    i. Surface → split surface

10. EMS Sensors

a. Tibial plateau segment:
    i. Design first cylinder
        1. Diameter = 7
        2. Boolean union to caudal proximal tibia
        3. Center between the caudal most points of the medial and lateral plateau
    ii. Design second cylinder centered within first
        1. Diameter = 1.8
        2. Boolean subtract second cylinder from first
            a. Depth = 5
b. Distal tibial segment:
    i. Parallel to sagittal axis
    ii. Design point at level of distal tibial crest
    iii. Create cylinder based on this point
    iv. Depth = to the level of medullary canal
    v. Diameter = 1.8
c. Align cylinders with sagittal axis:
    i. Plane to plane align
    ii. Plane on fixed entity = mechanical axis
    iii. Plane on moving entity = flat surface of cylinder plane
    iv. Method = coincident
d. Alter coordinate system of cylinder (update OCS)

i. Method = user defined

ii. User defined = mechanical axis plane

iii. Align cylinder → interactive translate → object coordinate system

11. <u>Model-Specific Cast</u>

a. Duplicate each tibia (uphill, normal, downhill)

b. Must use the tibia without screw holes

c. Must use segments that are filled in (close all holes)

i. Fix → fill hole freeform → entities = contour → advanced → automatic → triangulation = fine → unclick tangent

ii. Alternative: fill hole normal function

d. Must use filled in medullary canal

i. Right click → separate → shells to parts (for entire tibia)

ii. Open surface list for individual proximal and distal parts in object tree

1. Erase medullary surface

e. Update the tibia coordinate system

i. Update OCS to CS → entity = tibia

1. Method = user defined coordinate system

2. User defined coordinate system = select sagittal plane

f. Model is ready for boolean subtraction from cast

g. Creating cast:

i. Design → create block primitive → method = around part

1. Entity = tibia

2. Method = margins

ii. Margins for normal cast:

    1. Negative x = -7.5
    2. Positive x = -2
    3. Negative y = -1
    4. Positive y = -7.5
    5. Negative z = 5.5
    6. Positive z = -15.5

iii. Margins for downhill cast:

    1. Negative x = -8
    2. Positive x = -1
    3. Negative y = -1
    4. Positive y = -6 .5
    5. Negative z = 5.5
    6. Positive z = -15.5

iv. Margins for uphill cast:

    1. Negative x = -7
    2. Positive x = -1
    3. Negative y = -1
    4. Positive y = -8
    5. Negative z = 5.5
    6. Positive z = -16

v. Margins for cylindrical base cast:

    1. Negative x = -2

2. Positive x = 5
3. Negative y = 5
4. Positive y = 5
5. Negative z = 8
6. Positive z = -20

h. Translate tibial plateau segment 1 mm from distal segment
    i. Use inertia axis for even translation
i. Boolean subtraction of each tibial segment separately from cast
    i. No clearance
j. Creation of cast screw hole guides:
    i. Diameter = 5
    ii. Create cylinder as previously described for screws, following screw trajectory
k. Trim model-specific casts
    i. Trim tool → delete inner

12. <u>Tibial Shift and Tibial Plateau Translation</u>

a. Tibial shift
    i. Align → interactive rotate
        1. Rotate about x-axis (red plane) – 5° shift
b. Tibial plateau translation
    i. Separate proximal tibial segment (separate shells to parts)
    ii. Align → translate/rotate → main entity = proximal segment
        1. Transformation = translate

2. Method = OCS (to preserve alignment)
3. Enable snapping = check
4. Translation step = 1

iii. Translate 3 steps (3 mm) medially

CHAPTER 2

DEVELOPMENT OF MOTION SENSOR ANALYSIS

Introduction

Tracking systems are an essential component of many medical, biomechanical, robotic and industrial technologies[7,8], optical and electromagnetic tracking systems are frequently utilized for these purposes. Optical tracking systems (OTS) are based on capture of light within the visible spectrum (videometric) to calculate target position (i.e., pose)[8]. Electromagnetic tracking systems (EMTS) rely on a generated magnetic field communicating with a nearby sensor composed of several coils. Based on this magnetic field, the sensors will then create a specific voltage and their position as either static or dynamic in the local environment can be traced[8].

Optical tracking systems date back to World War II and are used in a wide variety of applications today. This includes navigational surgery of the sinuses, dental arcade and spine, arthroplasty of the knee and hip and mitral valve reconstruction[8]. The OTS is composed of three main system “controls”: the optical cameras, sensors or markers for motion detection and a central unit to process this motion information[8]. There are two main configurations for camera placement in this system. The first consists of placing the cameras within the target itself, otherwise termed “inside-looking-out”. The second, an “outside-looking-in” approach, relies on placing the cameras in the local environment[8]. The latter is more commonly used in biomedical scenarios and was the protocol utilized during pilot testing of the Vicon equipment in this research. The markers, or sensors, placed on the target object are either passive, where they transmit information via reflection, or active, where information is passed to the control unit using energy emission[8]. In this phase of our work, we use spherical retroreflective (passive) markers with four cameras placed in the local environment. When using passive markers in an

OTS system, a minimum of three markers must be placed within a known geometric pattern to be able to track the target object with six degrees of freedom (DoF)[8]. This includes three translational and three rotational parameters, ensuring requirements of a 3-Dimensional coordinate system are met.

Electromagnetic tracking systems were first described in the 1970's by Wynn et al[9]. Today, EMTS are used mainly for tracking of surgical instruments, cardiac mapping, endoscopy, radiotherapy and to aid with specific orthopedic implant placement such as an interlocking nail within the medullary canal of a long bone[8,10]. There are three main components of the EMTS: the field generator or transmitter, sensors and a control unit which integrates the magnetic data[8]. The field generator acts as the reference coordinate system and produces a magnetic field specifically designed to be based on internal geometry[10]. Inductors are placed within the field at a specific orientation, most commonly in a tetrahedron shape but their orientation can be altered based on tracking environment. The sensors come in a wide variety of sizes and shapes, with the most common consisting of small coils surrounded by a protective sheath. They are typically connected to the control unit by thin wires. There are three general types of EMTS employed today: alternating current (AC)-driven, direct current (DC)-driven and passive[8,10]. In this research, a DC-driven system (trakSTAR – NDI) was used. A DC-driven system minimizes eddy currents, which are currents generated within the coils of the sensor that produce their own magnetic field unrelated to the field generator[8]. Eddy currents may be a source of error that is inherent within the AC-driven system[8].

There are limitations to both optical and electromagnetic tracking systems. Optical tracking systems rely on direct visualization of the target object by the camera equipment,

termed “line-of-sight”[8,10]. If any break in line-of-sight occurs during tracking, accuracy of the system decreases. Other limitations include interference from thermal and optical changes in the environment[8]. However, OTS’s have evidence for high repeatability and precision if used in the right setting[7]. They are also very useful for large-scale tracking, such as instrument guidance during surgery. On the other hand, the main limitation to an EMTS is interference with ferromagnetic objects within the local environment or on the target[8,10]. Of note, this research involves use of a 316L stainless steel TPLO plate (DPS) made of low-carbon grade steel. Specifically, this type of stainless steel is termed austenitic, as it is composed of a high amount of austenite that forms a carbon-based iron and thus is not ferromagnetic[11]. Another limitation of the EMTS is the constraint of tracking within the allowed area of the field generator[10]. The field generator chosen for this study had a tracking range of 660 mm (trakSTAR – NDI). Benefits of the EMTS include tracking without reliance of line-of-sight (i.e., within objects such as bones or tissues) and capturing movement within a small scale[8]. EMTS sensors are small and versatile, permitting placement within a minute target area of the object to limit interference of other aspects of the construct.

Both optical and electromagnetic tracking systems have been assessed for accuracy, precision and repeatability. Accuracy consists of mechanical and overall application correctness. Mechanical accuracy reflects the internal precision of the tracking system, whereas application accuracy illustrates the correctness of the equipment in relation to the local environment[8]. Precision involves the similarity of results during a test setting, and repeatability is the ability of the tracking system to reproduce similar results during different test settings[8]. In the literature, both tracking systems show good test

accuracy for their respective applications[7,8,10]. However, direct comparison is difficult due to lack of control of a multitude of variables within these studies. The trakSTAR EMTS system utilized in this study has been shown to have a positional accuracy of 1.4 mm and an orientational accuracy of 0.5°[10]. The transmitter used in this research is considered mid-range (as compared to short-range) and relies on a large working volume of 310 x 460 x 300 mm^3 compatible with 1.8 mm sensors and six DoF[8]. The working volume represents the area where tracking is possible.

Sources of error are present for both optical and electromagnetic sensors. For the OTS, these include large sizes of the reflective markers when collecting data from a small target object (due to noise artifact), improper marker placement on the target object (away from line-of-sight), poor calibration of the system and low camera resolution[8]. For the EMTS, sources of error include inherent equipment error, magnetic field interference (ferromagnetic materials) and eddy currents[8,10].

Optical Tracking System – VICON

In the initial phase of motion analysis of this research, pilot testing was performed using a Vicon optical tracking system. The printed bone models were instrumented with an array of three retroreflective markers mounted on custom designed frames featuring three orthogonal branches (**Figure 2.1**).

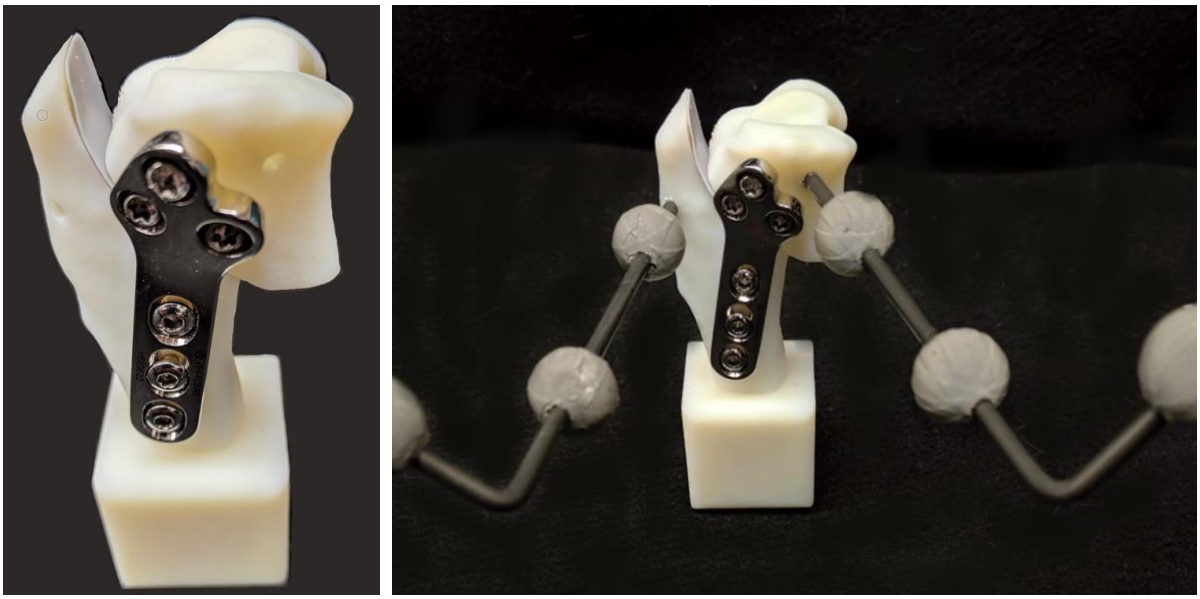

Figure 2.1. Illustration of early design of a pilot model with a downhill osteotomy and an inclined bone plate with an optical tracking system affixed

Left – Early pilot model with a downhill osteotomy and an inclined plate, featuring the original square base. **Right** – Same model affixed with a series of Vicon reflective markers on both distal and proximal tibial segments.

In a second series of tests, a 3D marker assembly was designed (Materialise 3-Matic, Leuven, Belgium) and 3D printed with tough resin (Formlabs Form2, Somerville MA, USA). The marker spheres designed within the 3D assembly were affixed with retroreflective tape. Each marker construct was placed in a drilled pilot hole on each segment of the model (tibial plateau segment and distal tibial segment). The relative spatial position of each marker array was captured by four Vero 1.3 Megapixel optical motion capture cameras (Vicon Motion Systems, Inc. Centennial, CO, USA) at a rate of 250 Hz (**Figure 2.2**). The 3D printed marker array was not captured with a high-resolution during calibration, thus all pilot models were equipped with the original retroreflective marker and frame construct. After successful calibration, the models were considered complete for testing.

Figure 2.2. Photograph depicting the testing set-up of the Vicon optical tracking system

Four cameras (one not pictured) were arranged around the Instron servohydraulic testing machine. A specimen has been equipped with retroreflective markers to recognize tracking of the tibial plateau segment in relation to the distal tibial segment during loading. Notice the electrical tape placed over the model and Instron loading frame in an attempt to reduce reflection of these objects and noise artifact.

Each instrumented model was mounted into the loading frame of an Instron servo-hydraulic testing machine (Instron model 1331: Instron Corp, Canton, MA, USA). To allow for unconstrained motion of the constructs during loading, the specimen base was secured to a custom designed X-Y table with a stainless-steel hollow cube fixture accepting the earliest designed loading block (**Figure 2.3**). The Instron actuator was equipped with a 2,225 N load cell (Model 1010AF-500: Interface, Scottsdale, AZ, USA) coupled to a 19.05 mm diameter steel sphere which articulated with the designed spherical defect of the tibial plateau segment. Specimens were tested non-destructively in compression from 5 N (preload) up to 300 N (10 cycles in a sinusoidal wave form). This load corresponds to approximately 1.2 times the body weight of an average 25 kg dog as modeled in the study. Tests were conducted under load control at a displacement rate of 1 mm/sec and a rate of 1 Hz.

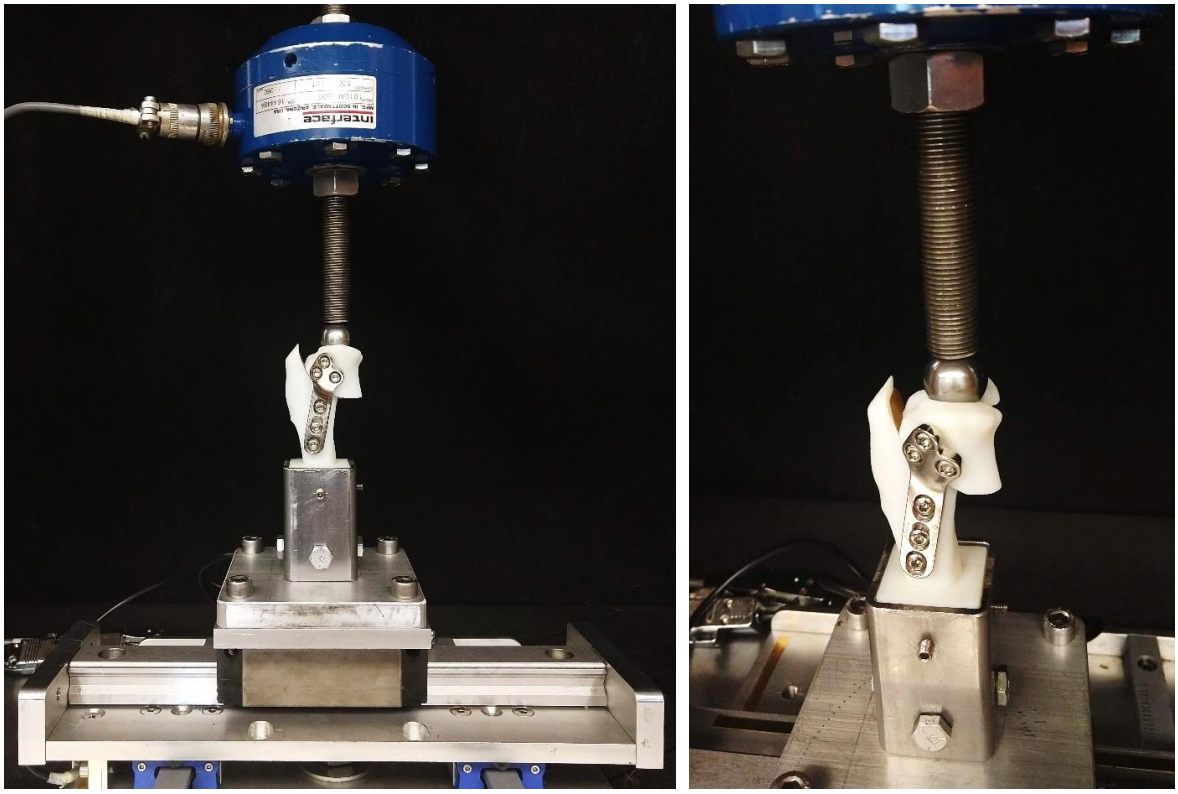

Figure 2.3. An early 3D printed model loaded into an Instron servohydraulic testing machine

The base of the model is locked into the table of the Instron which provides freedom in the X-Y axes. A steel loading sphere coupled to the Instron actuator has been aligned with the spherical depression on the specimen.

Pilot testing showed subjectively larger displacement with inclined plate models as compared to straight plate models by gross assessment. However, data acquisition of the tibial plateau segment in relation to the unconstrained distal tibial segment required matrix transformation with data output that necessitated extensive training by the operator. Data conversion was found to be time consuming and potentially fraught with inaccuracies from data collection with artifact interference. Thus, the use of OTS was abandoned and investigation of an electromagnetic tracking system was undertaken in the second phase of motion analysis of this project.

Electromagnetic Tracking System – trakSTAR

During the second phase of motion analysis, Northern Digital Inc (NDI) was used for all electromagnetic tracking (**Figure 2.4**). Initial calibration of the EMTS involved utilization of a high precision goniometer equipped with a custom-built stage to accept the electromagnetic sensors (**Figure 2.5**). The precision dual-axis goniometer allowed movement in roll and tilt with a 12.7 mm distance to its center of rotation (ThorLabs, Newton NJ, USA). The base of the goniometer was coupled with a precision X-Y-Z platform containing an addition internal/external rotational axis (ToAuto, Guangdong, China). A custom-built stage was designed and 3D printed (**Figure 2.6**). It was coupled at the top of the goniometer and accepted electromagnetic sensors for calibration testing (**Figure 2.6**). The square base of the stage had dimensions of 25 x 25 x 2 mm. The cylindrical hollow top had a diameter and height of 20 mm. Four pilot holes were designed on each consecutive corner of the square base with a diameter of 2.26 mm. Four additional pilot holes were created midway along the cylindrical top and equidistant along its circumference. Each had a diameter of 1.8 mm to accept an electromagnetic sensor. A fifth pilot hole of the same diameter was made at the center of the cylindrical top.

Figure 2.4. Illustration of the electromagnetic tracking system

Left – Control unit; **Center** – Transmitter box (i.e., field generator); **Right** – Electromagnetic sensor. Coils are placed within a protective outer sheath (1.8 mm diameter) as shown. *Image source: NDI, Waterloo Canada*

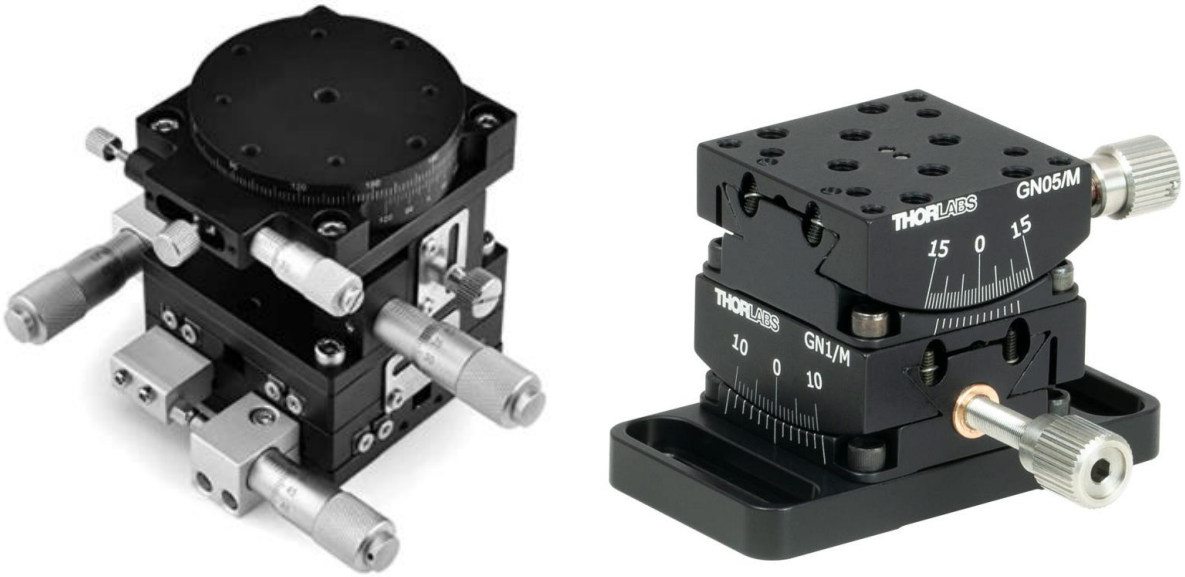

Figure 2.5. Components of the six DoF test construct used for calibration of the electromagnetic tracking system

The precision X-Y-Z platform with additional internal/external rotational freedom (*left*) is coupled to the precision dual-axis goniometer which permits movement in roll and tilt (*right*). A total of six DoF (3 translational, 3 rotational) are controlled with this construct.

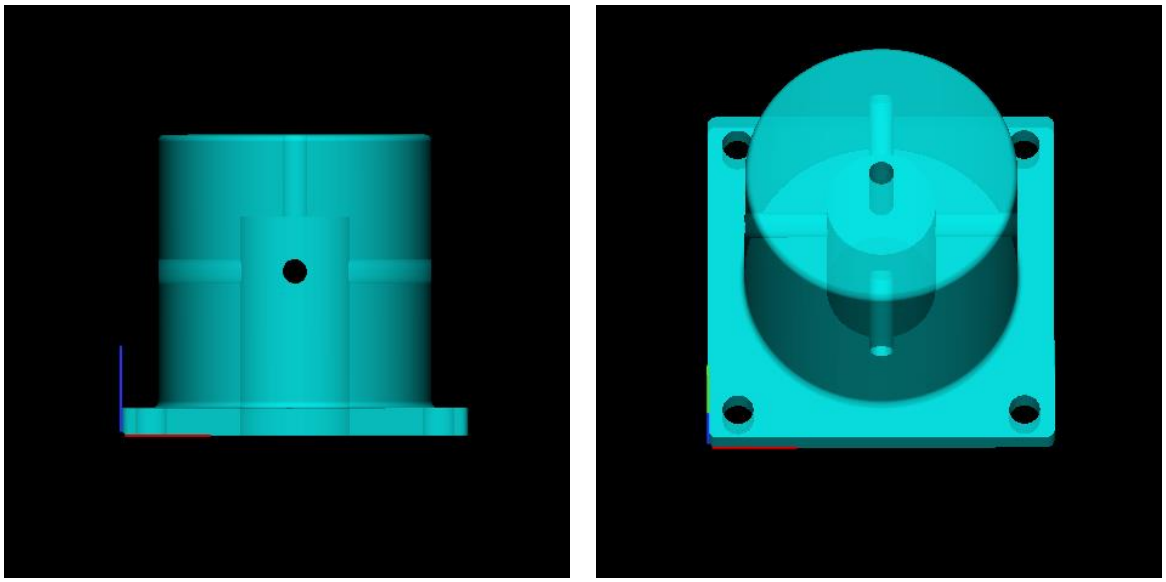

Figure 2.6. 3D design of the top stage of the goniometer to accept electromagnetic sensors

A cylindrical 3D printed stage was designed to include pilot holes to accept the electromagnetic sensors. Manual movements of the X-Y-Z platform and goniometer result in an equivalent displacement of the sensors.

The coupled X-Y-Z platform and goniometer (**Figure 2.7**) was placed on a table adjacent to the transmitter box (i.e. field generator) and one electromagnetic sensor was secured to a pilot hole during each test (**Figure 2.8**). All translational and rotational displacements were manually performed by a single operator to a set distance that was blinded to the second operator of the control unit. A static data point of the sensor displacement was obtained by the second operator and recorded. This was then validated by the first operator as accurate or inaccurate. All positional and rotational displacements were validated and shown to be accurate (**Table 2.1**). Based on this calibration, the direction of translation and rotation was recorded in relation to the transmitter box for future reference.

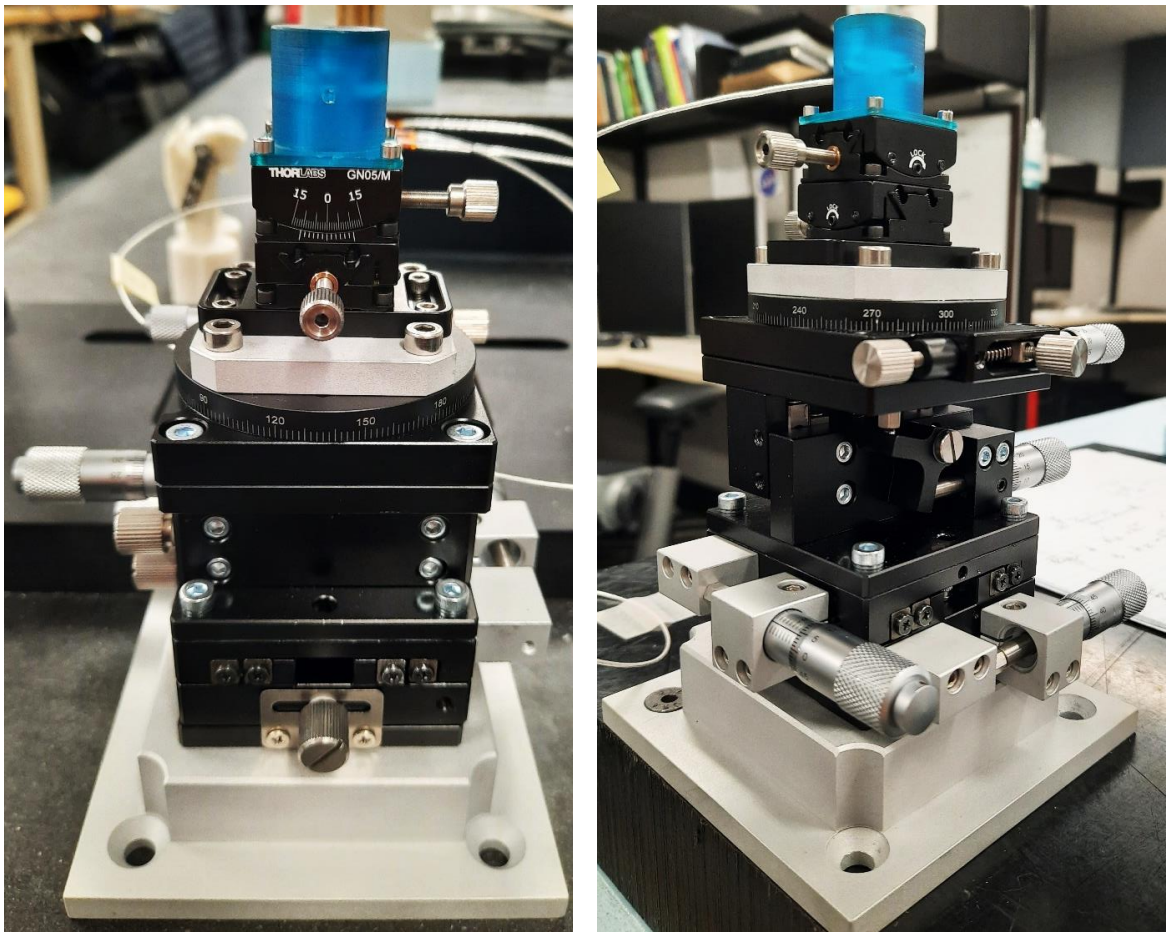

Figure 2.7. Coupled X-Y-Z platform and goniometer for calibration testing of the electromagnetic tracking system

The precision X-Y-Z platform (*bottom of construct*) is coupled to the precision dual-axis goniometer (*top of construct*). The 3D printed stage to accept electromagnetic sensors is shown screwed onto the goniometer (*blue*).

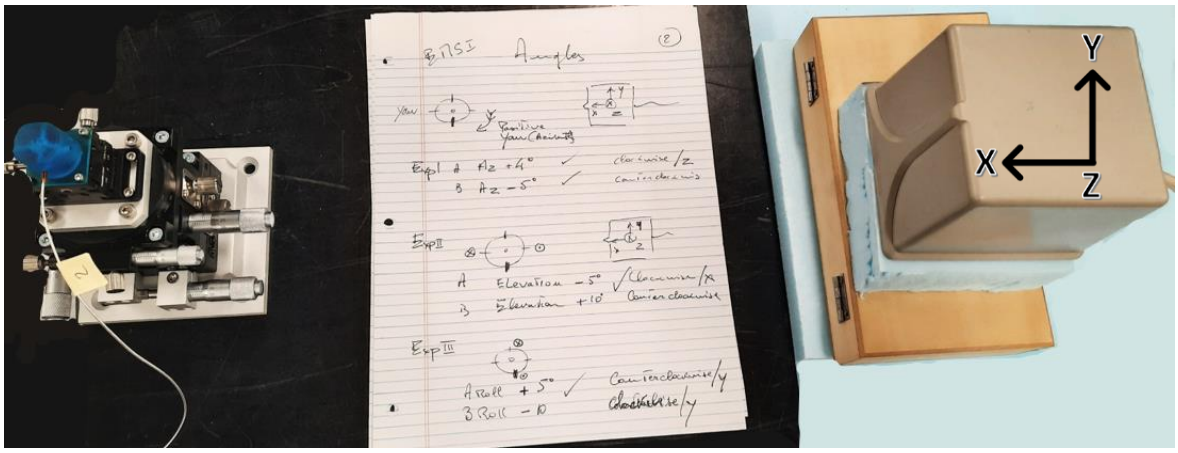

Figure 2.8. Set-up of the goniometer calibration experiment

The field generator was placed adjacent to the goniometer construct and remained static throughout the study. Notice the single electromagnetic sensor placed within the goniometer stage. As the goniometer is moved manually and data is acquired, translational and rotational displacements as well as their directions were recorded to compare their relationship to the global coordinate system within the field generator.

Translation			
Experiment	**Direction**	**Distance (mm)**	**Validation?**
A	X	2	Yes
B	Y	2	Yes
C	Z	2.3	Yes
D	X, Y, Z	3, 1, 2.5	Yes
Angulation			
Experiment	**Direction**	**Rotation (degrees)**	**Validation?**
E	Internal/External Rotation	+4	Yes
F	Internal/External Rotation	-5	Yes
G	Rock-Back	+5	Yes
H	Rock-Back	-10	Yes
I	Roll	-5	Yes
J	Roll	+10	Yes

Table 2.1. Calibration results for EMS validation

Accuracy of the EMS was validated along six DoF. As one operator manually translated/rotated the goniometer a predetermined distance, a second operator ensured accurate output of this movement at the central processing unit.

Discussion

Initial optical tracking with the Vicon system during loading showed visual displacement of the tibial plateau with data output through the software. However, there were several limitations using optical tracking during load testing. The first was noise reflection from adjacent objects including the construct base, Instron support beams, spherical actuator and the TPLO plate. Thus, during pilot testing two methods to reduce noise were attempted. The first was to cover the model and implant components with a coat of matte paint. The second involved covering the implant and adjacent reflective structures with black electrical tape (**Figure 2.9**). With both methods, noise was persistently picked up by the Vicon system and the retroreflective markers had poor resolution.

The second limitation of the Vicon optical tracking system was data acquisition and analysis. Due to unconstrained motion of the specimen base along the X-Y table, displacement was recorded between both moving construct markers in relation to a global coordinate system. Specific displacement of the tibial plateau segment required complex matrix transformation with the potential for error and loss of displacement data on a microscale. In addition, extensive training was required to understand the complexities of data acquisition with this system. Therefore, an alternative, namely an electromagnetic tracking system, was investigated.

For electromagnetic tracking, a custom-built press with a fixed base to accept the model was utilized. The electromagnetic tracking system was calibrated and checked for accuracy with a precision goniometer as described above. During pilot testing, no additional noise was perceived from the local environment, particularly from the plate

mounted onto each model. The press, EMTS and specimens were placed in an environment with no nearby ferromagnetic objects. Acquisition of displacement data was feasible and required no data transformation as each electromagnetic sensor was oriented in reference to the field generator global coordinate system.

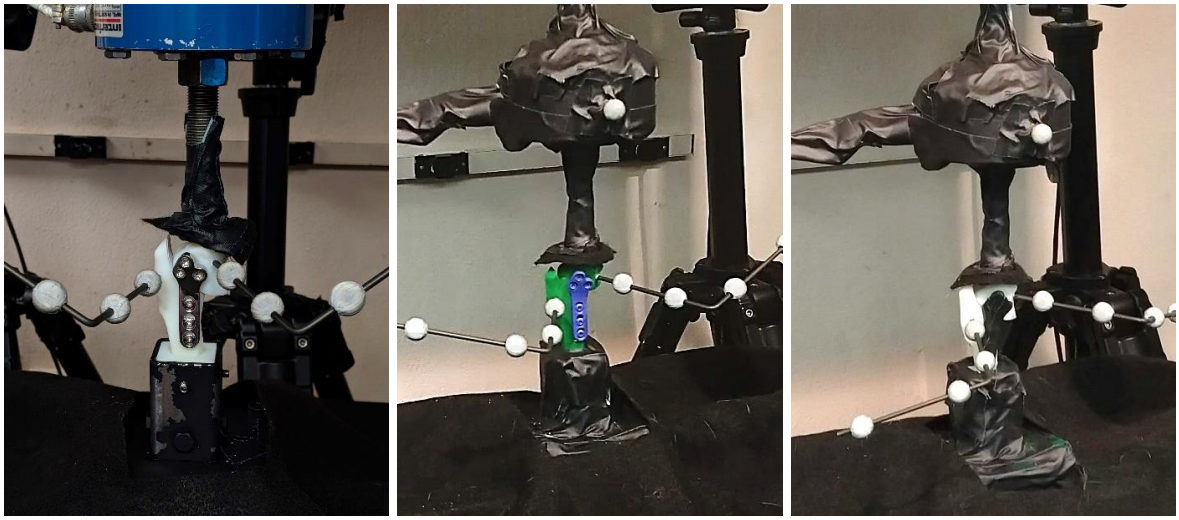

Figure 2.9. Three alternate methods attempted for optimal tracking data acquisition

Left – Natural specimen created a significant amount of noise artifact due to the reflection of the TPLO plate with the Vicon markers. **Center** – Painting of the specimen and TPLO plate did not reduce noise artifact. **Right** – Electrical tape placed over the bone plate reduced, but did not eliminate noise artifact.

CHAPTER 3

EFFECT OF LOADING LOCATION ON TIBIAL PLATEAU ROCK-BACK

Introduction

The mechanical axis of any long bone is measured in relation to its proximal and distal joint centers[12]. After defining these anatomical landmarks, a straight line connecting the two points is drawn. When performing a biomechanical study simulating *in vivo* conditions, it is important to identify and apply loads along the mechanical axis as this is the primary load sharing axis of the bone.

The mechanical axis of the tibia is measured on radiographs when the tibia is positioned parallel to the cassette with the X-ray beam centered on the tibial tubercles[12]. Placing the hock and stifle joints at 90° flexion facilitates accurate identification of proximal and distal joint centers[12]. A straight line is drawn from the center of the tibial tubercles along the tibial plateau to the center of a best-fit circle of the talus (**Figure 3.1**). The tibial plateau angle (TPA) can be measured from this axis by calculating the angle between the slope of the tibial plateau and a line perpendicular to this mechanical axis (**Figure 3.1**.) In this study, the TPA was measured at 32°; thus to achieve appropriate leveling of 5° following TPLO, the tibial plateau was rotated 27°[13,14].

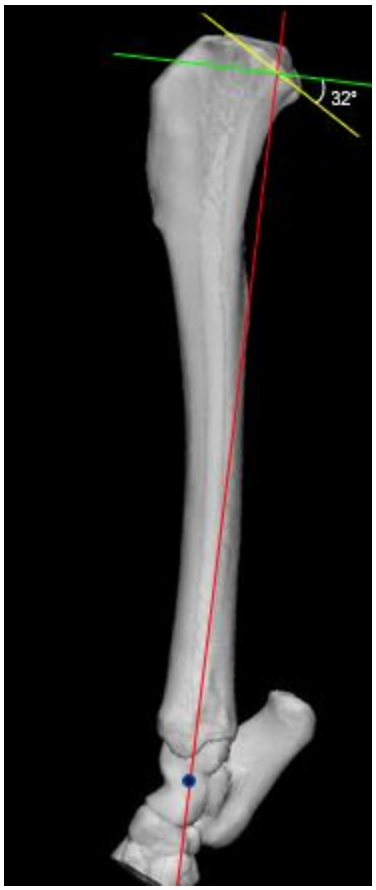

Figure 3.1. Determination of the tibial mechanical axis in the dog using a CT-based tibial model

The tibial mechanical axis is determined by a line (*red line*) centered over the tibial tubercles proximally and the center of the talus distally (*blue point*). A second line is drawn indicating the medial tibial plateau (*yellow line*). The TPA is then measured at the intersection of this tibial plateau line and a line perpendicular to the tibial mechanical axis (*green line*).

The aim of this phase of research was to assess the influence that loading location has on the magnitude of rock-back. Although the final experiment involved testing all models along their tibial mechanical axes, we surmised that rock-back is an irreversible phenomenon whereby the loading center shifts caudally along the tibial plateau, further increasing the magnitude of rock-back. Thus, we wanted to test this hypothesis.

Rock-back is a result of TPLO fixation failure with loss of osteotomy reduction occurring post-operatively, ultimately leading to increased TPA. This may result in return of cranial tibial thrust and stifle instability. In a normal stifle, loads are applied at the center of the joint near the tibial tubercles as described above, which is slightly caudal to the centroid of the head of the TPLO plate. In this experiment, we subjectively defined the centroid of the head of the TPLO plate as an average point between the proximal screws. Once rock-back is initiated, persistent loading may lead to further cranial displacement of the tibia over time along with caudal displacement of the tibial plateau. As a result, the location of the load application should theoretically shift onto a more caudal position on the tibial plateau. We surmised that this increases the moment arm between the centroid of the head of the TPLO plate and the point of application of the load.

The moment arm, otherwise known as a lever arm, is the perpendicular distance between an axis and the line of action of a force[15]. In reference to this experiment, a longer distance between the plate centroid (the axis) and the tibial load (the line of action of the force) will result in a larger moment arm. Thus, as the load shifts to a more caudal location in relation to the centroid of the plate, rock-back should increase **(Figure 3.2).** Once this process is initiated, rock-back is likely an irreversible phenomenon with persistent caudal loading and a further increase in TPA, leading to catastrophic failure.

Conversely, if the load were applied in a more cranial location, the reduction in moment arm may result in a decrease in the rock-back magnitude. While this scenario is clinically impossible, it was nonetheless evaluated to test this theory.

Therefore, three scenarios were compared in this experiment – a cranial loading force, a central loading force (the tibial mechanical axis) and a caudal loading force. We hypothesized that the caudal loading site would have the largest magnitude of rock-back due to an increased moment arm. Conversely, the cranial loading site should have the lowest magnitude of rock-back. In addition, we hypothesized that this rock-back magnitude would be consistent regardless of plate inclination.

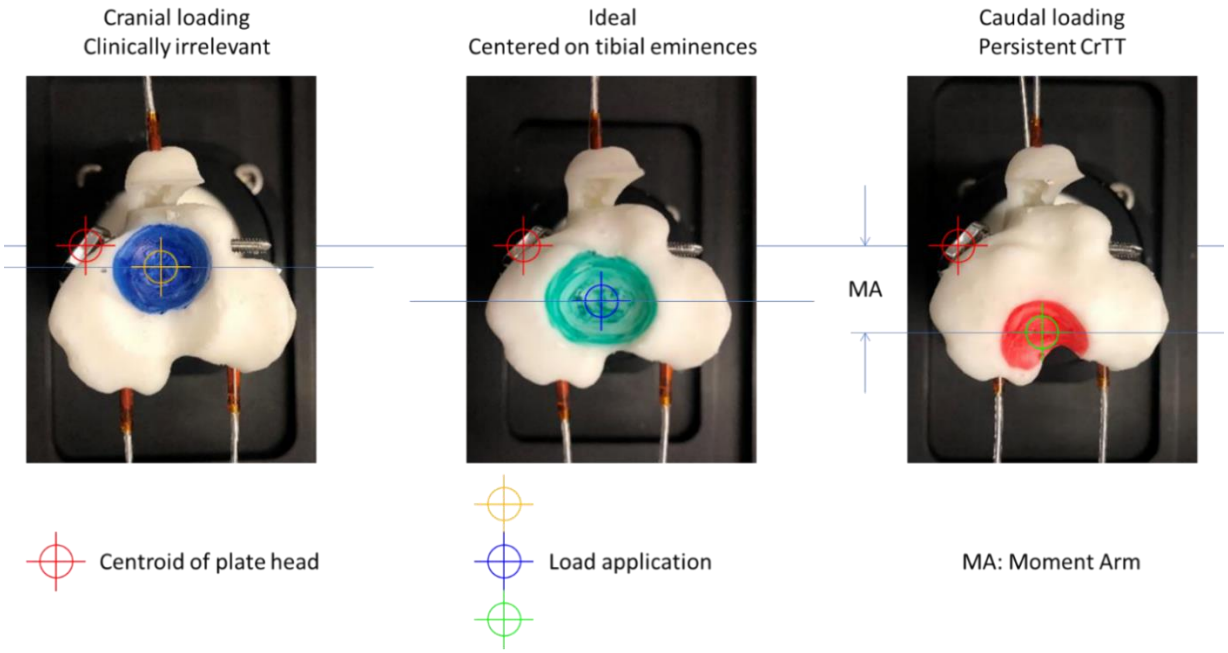

Figure 3.2. Illustration of the three tibial plateau loading locations and their effect on rock-back

Left – a cranially placed load has a short distance between the center of the proximal plate and the center of loading. Thus, the moment arm is reduced and rock-back is minimal. **Center** – the same specimen with a centrally placed load has a slightly longer moment arm and rock-back is approximately twice as large compared to the first condition. **Right** – a caudally placed load has the longest moment arm and therefore the greatest amount of rock-back.

Materials and Methods

In this experiment, there were three main groups corresponding to each loading location (cranial, central and caudal). Each group contained four samples, two with an inclined plate and two with a straight plate as described in chapter 1 of this research to assess whether the effect of loading location was consistent regardless of plate inclination. All samples were designed with a downhill osteotomy for control.

The central loading location was the reference point for the other two loading sites, namely a cranial and caudal loading site. This reference load corresponds to the mechanical (loading) axis of the canine tibia and was centered on the tibial tubercles. A spherical depression was designed into the tibial plateau using a spherical diameter of 19.05 mm recessed 50% into the tibial plateau. The cranial loading site was designed 8 mm cranial to the central loading site along the sagittal plane. The caudal loading location was translated 8 mm caudal from the central loading site in a similar fashion. Medial-lateral translation remained static.

The remainder of the model components were designed as previously described in chapter 1. Models were instrumented with electromagnetic sensors on each tibial segment, one on the tibial plateau segment and another on the tibial crest of the distal tibial segment. The models were mounted into a modified custom-designed table press for compression loading (**Figure 3.3**). The loading plate of the press was affixed with a universal joint connected to a brass loading sphere distally, allowing for unrestrained motion of the tibial plateau segment in all planes and about all axes (six DoF). The base of each model was rigidly coupled to the base of the press.

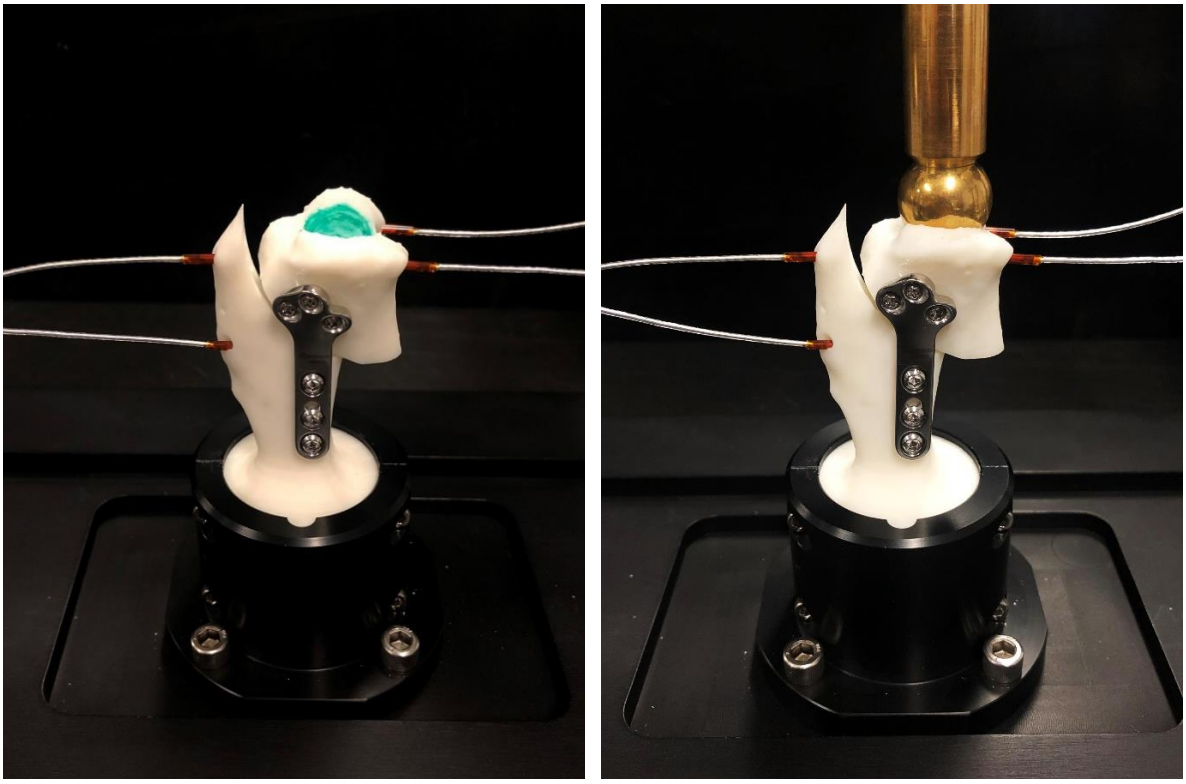

Figure 3.3. Model mounted into custom-built loading press during testing of loading location on tibial plateau rock-back

Left – A specimen is placed into the custom-built loading press with a spherical depression centered over the tibial tubercles. **Right** – Load is applied via a brass sphere centered on the custom-made depression on the tibial plateau.

Specimens were cyclically and non-destructively loaded to 200 N for four cycles using this custom-built loading press with manual placement of weights onto the press loading platform. This load corresponded to approximately 80% of the body weight of a 25 kg dog as represented in this research. The procedure for loading weights was as follows:

- Cycle 1
    - First reading – no weight placement to mark the baseline of the electromagnetic sensor locations
    - Second reading – manual placement of weights to 200 N followed by data recording of electromagnetic sensors locations
- Cycles 2-5
    - Unloading of weights occurred within 3-5 seconds of completion of the previous cycle and the first reading of the subsequent cycle was performed as described above

Angular displacements about the X (craniocaudal – valgus/varus), Y (mediolateral – craniocaudal tilt [i.e. rock-back]) and Z (proximodistal – internal/external rotation) axes were recorded. Specifically of interest was rock-back, or the displacement of the tibial plateau segment about the Y-axis in relation to the distal tibial segment. Mean rock-back between the six groups was compared using a two-factor ANOVA and Tukey's post-hoc pairwise comparison when significance was found ($p<0.05$).

Results

Mean ± standard deviation rock-back magnitude was 0.095° ± 0.111°, 0.608° ± 0.315° and 1.518° ± 0.791° for the cranial, central and caudal loading sites, respectively. While rock-back increased with caudal displacement of the loading site, the difference was only significant between cranial and most caudal sites (~ 1.4°) and between central and most caudal sites (~ 0.9°) ($p<0.05$). The mean rock-back difference between cranial and center loading locations was 0.50° and not significant despite showing a trend towards significance.

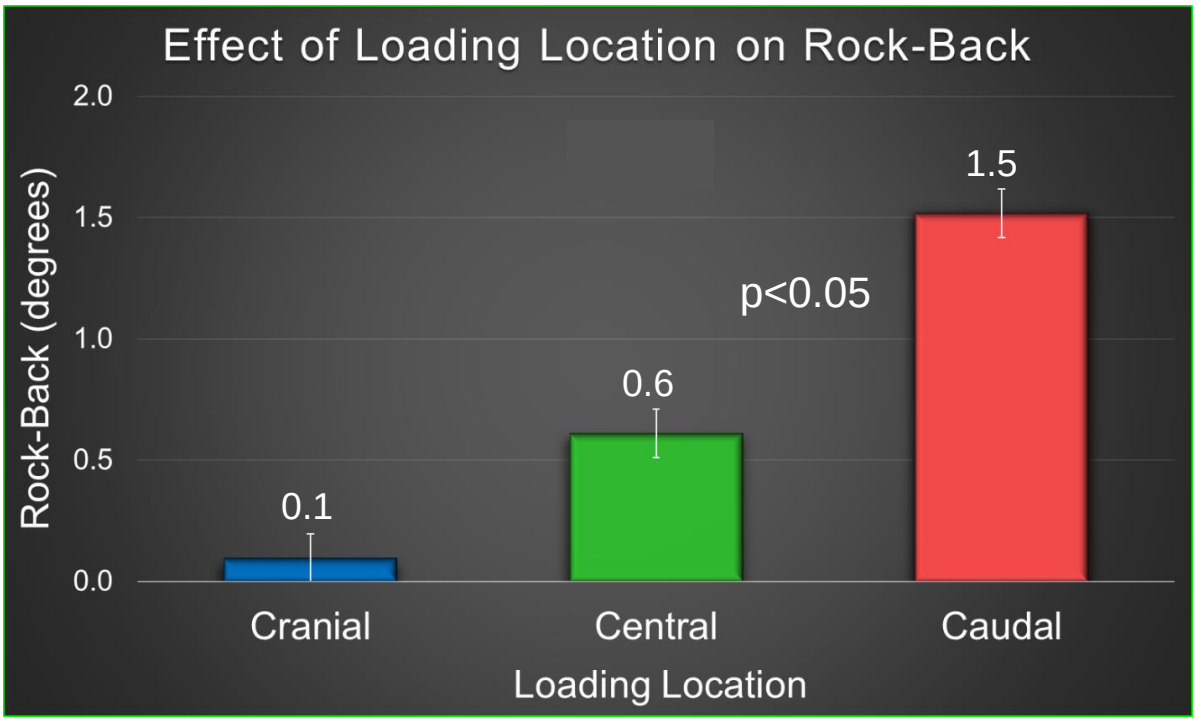

Figure 3.4. A histogram illustrating the effect of loading location on rock-back

The caudal-most loading location showed significantly greater rock-back magnitude compared to both the central loading location and the cranial loading location due to the largest moment arm between the load and the plate center ($p < 0.05$). There was no significant difference between cranial and central loading locations ($p > 0.05$).

Discussion

This pilot study demonstrated that rock-back of the tibial plateau varies with tibial loading location. The first hypothesis that the greatest magnitude of rock-back would occur with a caudally placed load was accepted. This rock-back magnitude was approximately 16 times greater than the most cranially positioned load. This result suggests that a larger moment arm between the centroid of the plate and the point of application of the load has a propensity to further increase displacement of the tibial plateau, leading to a greater degree of rock-back (**Figure 3.3**). Interestingly, although the cranial loading site showed consistently smaller rock-back compared to the central loading site, this difference was not significant. Because of a low sample size within each group, this may have been the result of a Type II error and a larger sample size could have shown significance.

There was not a significant difference between plate inclination within each loading group, accepting our second hypothesis. Because the proximal aspect of the plate, or the plate centroid, was located the same distance from the loading axis regardless of plate inclination, the moment arm should not change considerably when plate inclination is altered. On the other hand, a large translation of the loading axis away from the plate centroid considerably increases the distance between the plate and the load; consequently, the moment arm should increase correspondingly.

We speculate that when rock-back is initiated, two phenomena occur 1) the tibial plateau tilts in a caudal direction and 2) the tibia translates into a cranial direction. As a result, the load that was previously centered along the tibial tubercles now shifts along the caudal tibial plateau further from the plate centroid. As this load moves in a more

caudal direction with an increase in cyclical loading over time, the moment arm should increase even further. This results in an irreversible phenomenon that once begun has a compounding effect and further increases the overall magnitude of rock-back. Conversely, cranial loading theoretically creates a smaller moment arm between load application site and plate head centroid as verified in this experiment, thus minimizing rock-back magnitude. While this scenario does not occur clinically and thus is clinically irrelevant, it supports our hypothesis that rock-back increases with caudal displacement of the load application site.

After verification of the influence of loading location on rock-back, the next phase of this research involved placing the load directly along the true mechanical axis of the tibia for all samples, emulating the biomechanics of the canine tibia *in vivo*.

CHAPTER 4

EFFECT OF OSTEOTOMY AND PLATE ORIENTATION ON TIBIAL PLATEAU ROCK-BACK FOLLOWING TPLO USING A TIBIAL GAP MODEL

Introduction

Cranial cruciate ligament rupture is one of the most frequently diagnosed orthopedic conditions in dogs[16,17]. Appropriate treatment of cranial cruciate ligament disease in dogs is paramount for return of stifle function, limitation of osteoarthritis progression and reduction of pain. The intact cranial cruciate ligament functions to eliminate cranial tibial subluxation, limit tibial internal rotation and limit stifle hyperextension. With cranial cruciate ligament failure, forward motion of the tibia, otherwise known as cranial tibial thrust, ensues, resulting in lameness, osteoarthritis and discomfort.

While many cranial cruciate ligament rupture etiologies have been proposed since the early 1950's, tibial plateau leveling osteotomy (TPLO) is currently the most common high-tibial osteotomy technique for stabilization of the canine stifle joint[18-21]. During the stance phase of the gait cycle, the cranially oriented component of the joint force, termed cranial tibial thrust (CrTT) is opposed by the intact cranial cruciate ligament[14,20]. Alternatively, in a cranial cruciate ligament deficient stifle, the CrTT is left unopposed during weight-bearing, leading to cranial tibial subluxation and joint instability. Slocum described the linear relationship between CrTT and tibial plateau slope (TPS). Namely, a high TPS leads to a greater tibial plateau angle (TPA), which increases the magnitude of the CrTT and thus the forward motion of the tibia. Leveling the TPA, the premise behind the TPLO, not only eliminates this forward component of the joint force but reverses it to a caudally oriented shear force known as the caudal tibial thrust (CaTT) which is opposed by the caudal cruciate ligament[14]. This negates the need for an intact cranial cruciate

ligament and makes stifle stability dependent of the integrity of the caudal cruciate ligament (**Figure 4.1**)[22].

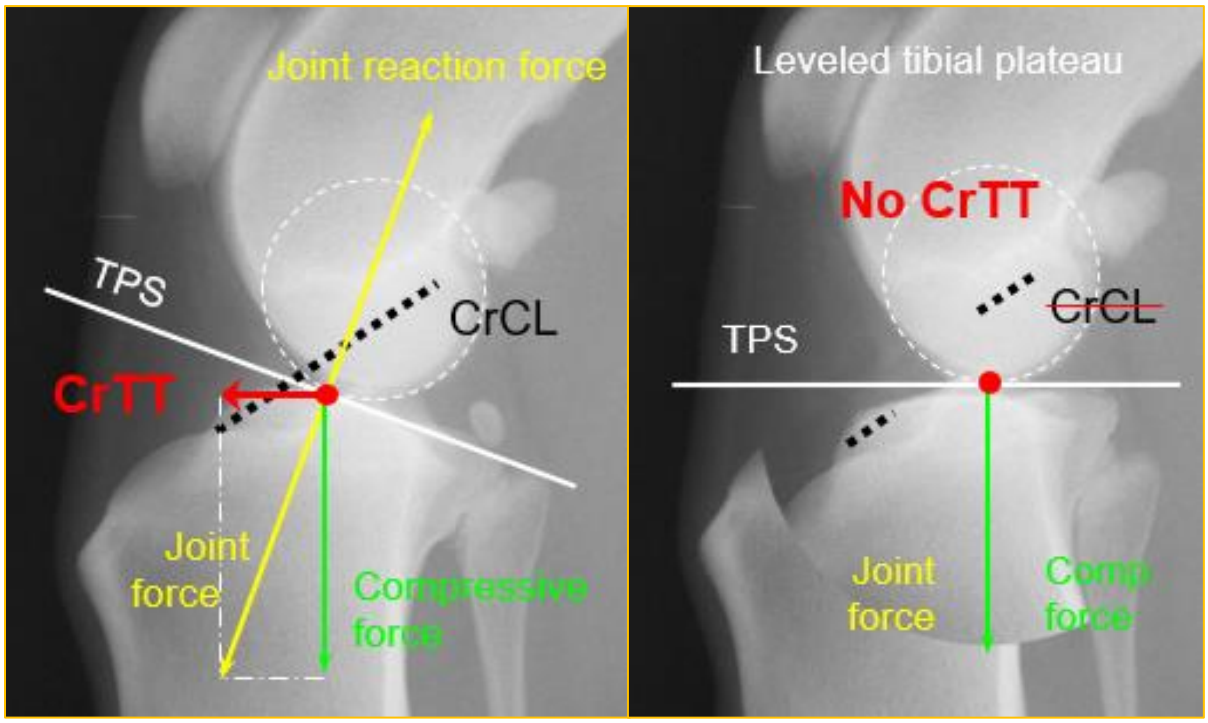

Figure 4.1. Diagram of the forces acting across the stifle joint

In a normal stifle (*left*) the cranial tibial thrust (CrTT – red arrow) is opposed by the intact CrCL (*black dotted line*). In the CrCL deficient stifle (*right*) after tibial plateau leveling, the CrTT is eliminated; the joint force is reduced to its compressive component (*green arrow*). Since the magnitude of the CrTT is proportional to the tibial plateau angle, accurate surgical planning and meticulous surgical technique are essential to the success of the TPLO procedure. Persistence of a tibial plateau angle greater than ~6.5° (as seen following rock-back) may jeopardize stifle stability. TPS: Tibial plateau slope. *Image courtesy of Dejardin LM. Chapter 148: Tibial Plateau Leveling Osteotomy. In: Slatter D. Textbook of Small Animal Surgery.*

Warzee quantified the effect of TPA on CrTT. With rotation of the tibial plateau, cranial tibial thrust was converted to caudal tibial thrust at a TPA of 6.5° in relation to the mechanical axis of the tibia. With increased rotation the magnitude of the CaTT increased thus placing undue stress on the caudal cruciate ligament. Confirming Slocum's clinical recommendation to maintain a postoperative TPA of 5°, a later study using a mathematical model showed this CrCL stress was present until a TPA of 5° was reached[23]. Therefore, during TPLO, a tibial plateau rotation to achieve a TPA between 5 to 6.5° is performed to strike a balance between stifle stability and limited caudal cruciate ligament strain[14,20]. Accurate planning and precise surgical execution are critical to the success of the TPLO.

Numerous TPLO complications have been reported since its introduction in 1993. The current post-operative complication rate varies from 9.7-34%, with a major complication rate of 3-15%[24-29]. Reported complications include tibial tuberosity or fibular fracture, patellar luxation/fracture, implant loosening/breakage, pivot shift, latent meniscal injury, surgical site infection, patellar desmitis and delayed or non-union of the osteotomy[30-37]. Tibial plateau rock-back is yet another complication that has been described in the veterinary literature, but no causative factors have been elucidated[1,17,38]. Rock-back describes a phenomenon whereby loss of reduction occurs post-operatively secondary to fixation failure. Under compressive forces, the tibial plateau segment tilts caudally, which leads to return of a high TPA and consequently, may result in return of CrTT and joint instability. Additionally, rock-back creates a cranial and proximal osteotomy gap that may cause tibial crest fracture due to loss of buttress support. Subsequent delayed or non-union may result in further loss of fixation, progressive

increase in degree of rock-back and ultimately implant failure and tibia/fibular fracture (**Figure 4.2**).

Figure 4.2. Radiographs of clinical cases illustrating the effect of tibial plateau rock-back

A – Immediate postoperative radiograph (*left*) illustrates inclination of the bone plate with respect to the caudal tibial cortex (TPA 8°). Eight-week postoperative radiograph (*right*) illustrates tibial plateau rock-back with a TPA of 27° as well as fixation and bone failures. **B** – An inclined bone plate and cranial osteotomy gap (*left*) led to collapse of the tibial plateau and secondary fibular fracture under compressive load. Excessive stress on the implant eventually led to construct failure and tibial plateau rock-back (*right*).

There is a paucity of information in the peer-reviewed literature regarding causative factors of rock-back and thus, biomechanical studies are warranted. Errors in TPLO surgical technique are not uncommon and include laceration of blood vessels, severance of the patellar ligament or medial collateral ligament, intra-articular screw placement and tibial fracture[27]. However, none of these studies evaluate a correlation with rock-back. Several studies assessing the influence of implant type on rock-back have found conflicting results[39-41], with evidence of rock-back when using either locking or cortical screws. Another study demonstrated rock-back occurrence, but no causes were identified[38]. Elucidating causes of rock-back may provide guidance on how surgical technique may be optimized to limit this potentially catastrophic complication. Establishing standardized principles for bone plate and osteotomy placement is crucial for trainee and surgeon development and maintaining consistency of the procedure.

From a mechanical standpoint, optimal repair stability is achieved when the long axis of a plate is parallel to the loading axis of the bone (i.e., the tibial mechanical axis). Yet to optimize screw purchase in the widest part of the tibial plateau, TPLO plates are often oriented oblique to this axis. Under compressive loads, one could surmise that this inclination generates a disruptive force couple that could separate the tibial segments, thus potentially increasing the risk of rock-back (**Figure 4.3**).

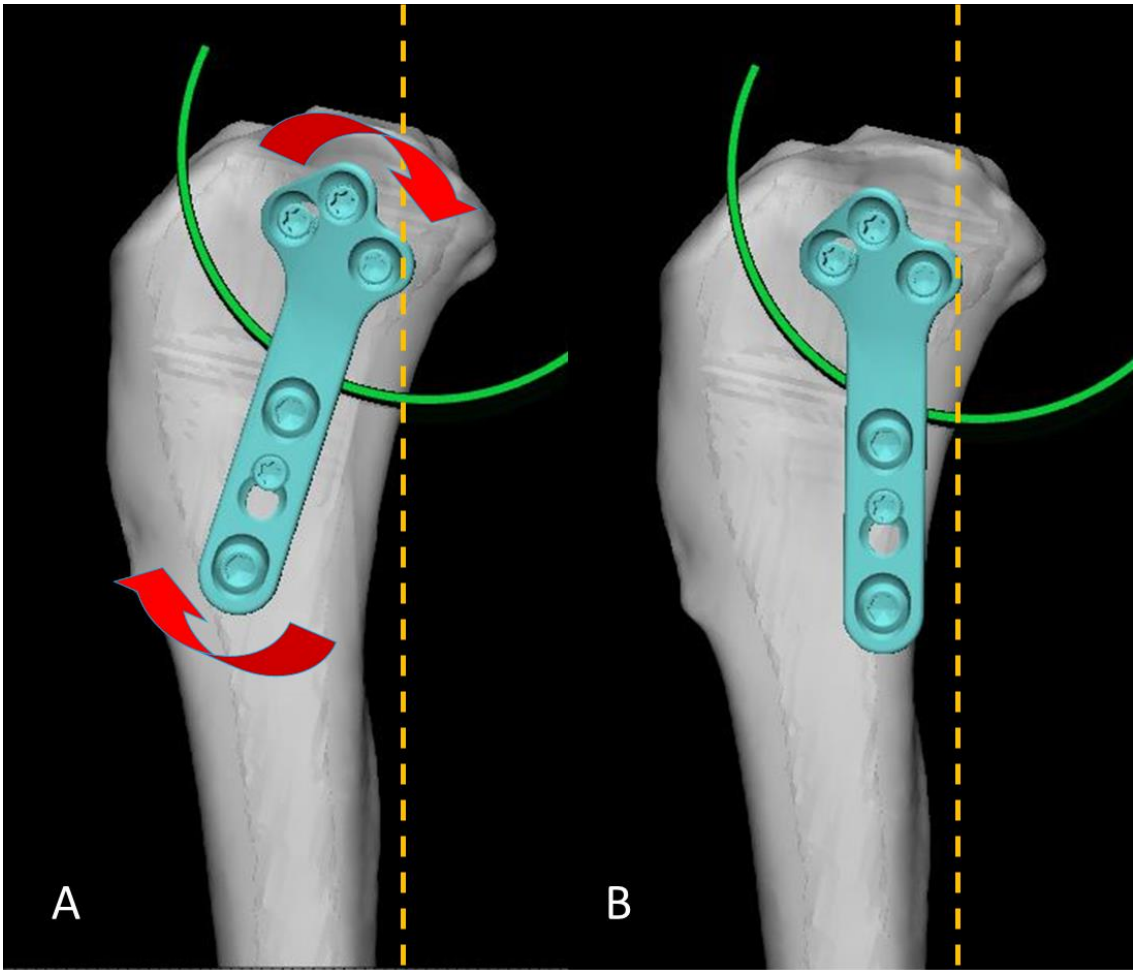

Figure 4.3. Illustration of the potential effects of two plate orientations on fragment stability

A – An inclined plate in relation to a line parallel to the caudal tibial cortex (*yellow dotted line*) may generate a disruptive force couple that increases the risk of rock-back. **B** – Conversely, by eliminating this couple, a plate orientation parallel to this cortex could reduce the risk of rock-back.

The orientation of the osteotomy in relation to the caudal tibial cortex (CTC) has been described as uphill, normal (i.e. perpendicular) or downhill. With an uphill cut, the proximal segment tends to center itself towards the lowest point of the osteotomy under compressive loads, which may theoretically increase interfragmentary stability as displacement of the tibial plateau segment beyond this point is constrained by the cut (**Figure 4.4 – A**). This osteotomy type is often achieved when using small diameter saw blades. However, rotation of the tibial plateau segment is reportedly considered more challenging. In addition, the smaller amount of bone stock proximally may lead to inadvertent intra-articular or intra-osteotomy screw placement. Conversely, with a downhill cut, interfragmentary shear forces may be generated during compression because the lowest point of the osteotomy is located at the exit point of the CTC (**Figure 4.4 – C**). In turn, this could predispose to rock-back. A downhill osteotomy is often achieved with a larger saw blade and thus generates a larger tibial plateau segment which in turn facilitates bone purchase. Downhill cuts are often performed intra-operatively as it is reported by some surgeons to facilitate rotation of the tibial plateau. Therefore, an inexperienced surgeon may be more likely to perform a downhill osteotomy to minimize the demands of both bone plate application and tibial plateau rotation. A compromise between an uphill and downhill osteotomy could be achieved using a normal (i.e., perpendicular) cut, in which the osteotomy angle with the CTC is 90°. This may reduce interfragmentary shear forces while alleviating concerns for proximal screw purchase into a small tibial plateau segment (**Figure 4.4 – B**).

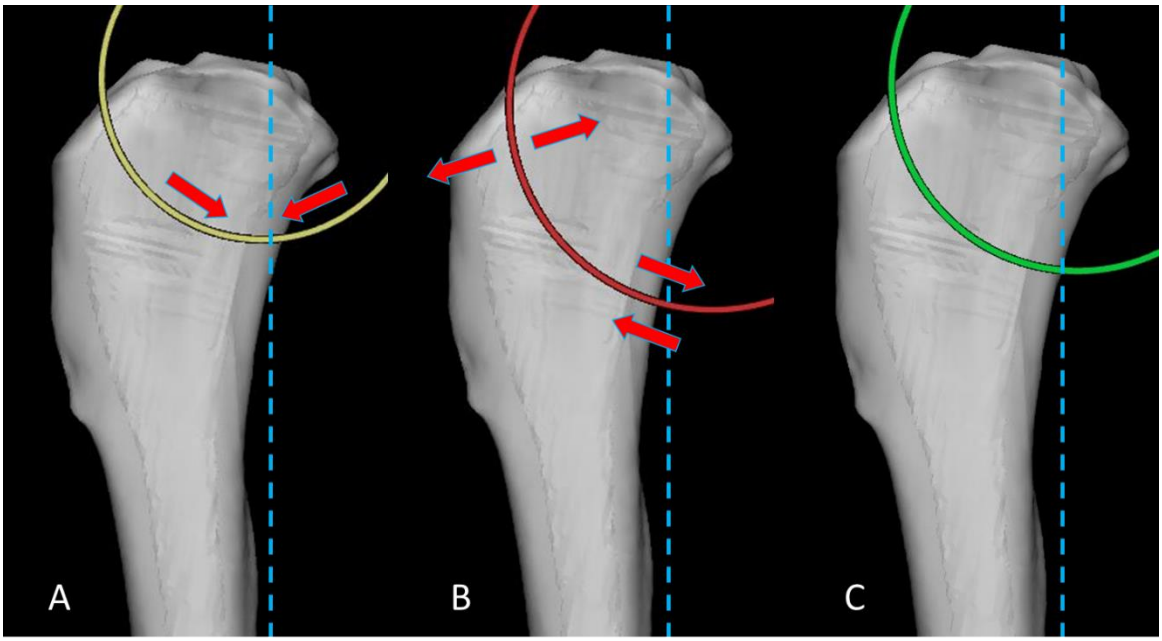

Figure 4.4. Illustration of the potential effects of three osteotomy orientations on fragment stability

A – *Uphill osteotomy* leads to the tibial plateau centering toward the bottom of the osteotomy and may improve postoperative stability under compression. **B** – *Downhill osteotomy* leads to a disruptive force couple which may promote fragment separation and shear along the inclined osteotomy, in turn leading to rock-back. **C** – *Normal osteotomy* may represent an optimal compromise between fragment stability and ease of tibial plateau rotation. Blue dotted line: line parallel to caudal tibial cortex.

The influence of plate and osteotomy orientation on rock-back remains a point of discussion amongst orthopedic surgeons. Two hypotheses regarding rock-back are evaluated in this study phase. The first hypothesis is that a plate placed at an incline to the tibial mechanical axis will have a larger degree of rock-back compared with a plate parallel to this axis. The second hypothesis is that a downhill osteotomy will result in greater rock-back magnitude than either a normal or uphill osteotomy. The ultimate goal of this study was to provide objective data to support recommendation for osteotomy and plate placement during TPLO, thus enhancing surgeon training and improving patient outcome.

Materials and Methods

The CT of a right tibia from a mid-sized dog (BW ~25 kg – BCS 7/9) was segmented and imported into design software (Materialise 3-Matic). Anatomical planes were established (sagittal, transverse, coronal) as well as the tibial mechanical axis. The proximal third of the tibia was digitally isolated and both a cylindrical base and a spherical depression centered on the tibial tubercles, to act as a coupling interface with a loading ball, were designed.

Three osteotomies were then created using saw blades of three different diameters. The osteotomy exit angle in relation to the caudal tibial cortex was measured along the distal osteotomy interface. The osteotomies were defined as uphill [saw diameter 21 mm – exit angle 75°], normal [saw diameter 24 mm – exit angle 90°) and downhill [saw diameter 27 mm – exit angle 105° **(Figure 1.4)**. The cranial osteotomy exit point in all models was located at the midpoint between the cranial footprint of the cranial cruciate ligament (CrCL) and insertion of the patellar ligament on the tibial tuberosity.

The proximal tibial segment of each model was then digitally rotated to a final TPA of 5° based on an initial TPA of 32°. The STL file of a 2.7 mm DePuy Synthes (DPS) TPLO plate with pre-placed screw trajectories was overlaid on the medial tibia. A 2.7 mm TPLO plate was chosen based on reported guidelines for plate placement. While the dog's body weight (25 kg) exceeds that commonly recommended for a 2.7 mm TPLO plate, the actual lean body was ~17.5 kg when considering a BCS of 7/9 corresponding to 30% body fat. A 2.7 mm TPLO plate is within the reported range for this weight based on DPS validation studies. In addition, bone size was taken into consideration when choosing the appropriate plate size. A 3.5 mm small TPLO plate did not fit on the uphill

models due to limited tibial plateau bone stock, whereas the 2.7 mm TPLO plate fit all constructs. Following digital plate placement, screw pilot holes were designed for both locking and cortical screws into the proximal and distal segments, respectively. Plates were placed at either a straight (0°) or 20° inclined angle in relation to the CTC. In total, six models were designed and included one osteotomy orientation (uphill, normal and downhill) for each plate inclination (straight or inclined).

A model-specific cast was created to maintain a 1 mm osteotomy gap during plate application. Models were printed on a resin-based 3D printer (Formlabs Form2, town, etc). Post printing, each model was placed into its respective cast and standard TPLO instrumentation was used to affix a 2.7 mm TPLO plate from DPS. All screws were secured at consistent torque by means of a calibrated torque screwdriver (1.50 Nm locking and 0.6 Nm cortical, respectively).

Models were instrumented with two electromagnetic sensors, one on the caudal tibial plateau and a second on the tibial crest of the distal tibial segment (NDI, Waterloo Canada). The models were mounted into a modified custom-built loading press[14] for compression loading (**Figures 4.5 and 4.6**). Iterations of the original limb press included an XY frame incorporated into the loading platform. In addition, the press actuator was coupled to the loading platform through a universal joint which free end featured a loading sphere matching the tibial plateau depression of each model. These modifications allowed unconstrained motion of the specimens during testing.

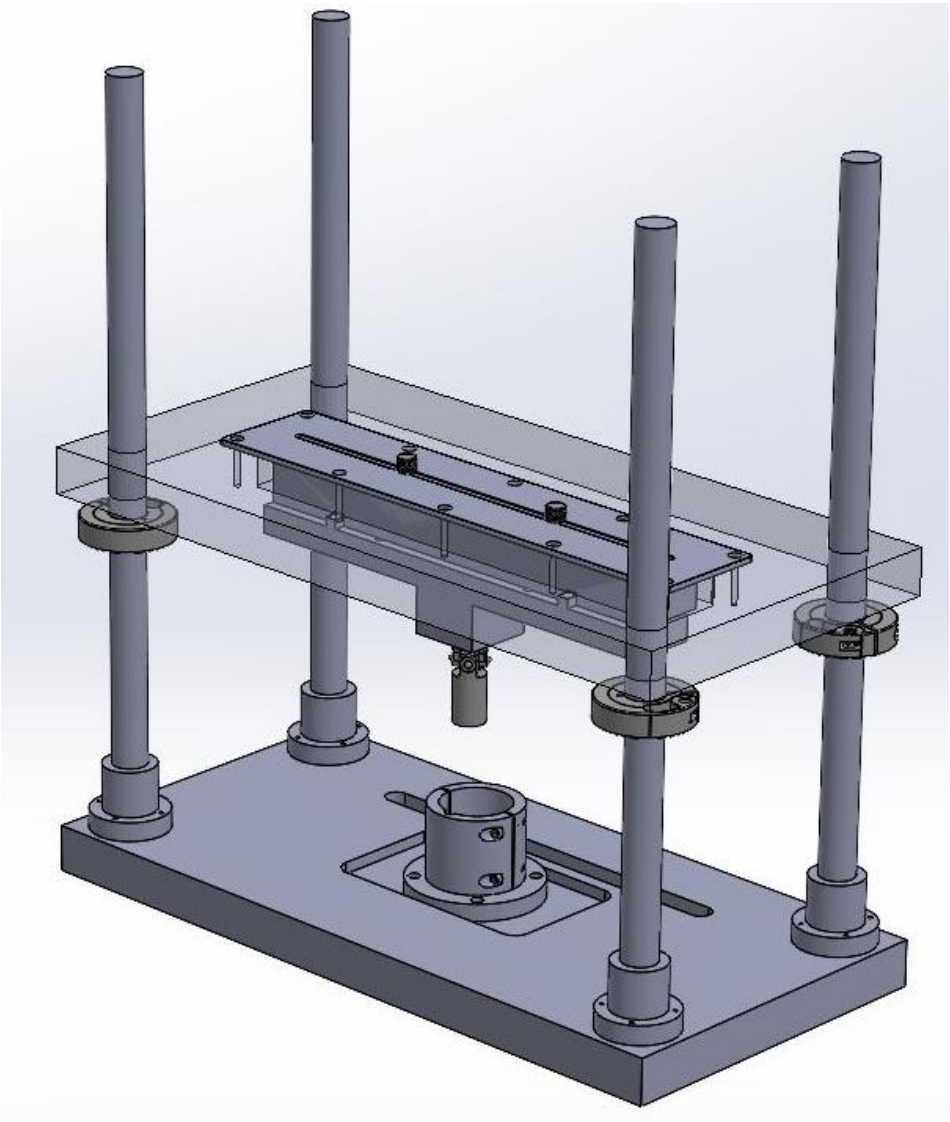

Figure 4.5. CAD assembly of the custom-built loading press including the proximal loading plate

The plexiglass loading platform is coupled to a universal joint via X and Y bars. The press actuator (not shown) features a loading sphere that is then coupled to the universal joint.

Figure 4.6. **Final custom-built loading press used in this study**

Photograph of the modified limb press showing the loading platform with fixtures allowing adjustments in the X and Y directions. The bottom fixture features a universal joint coupled with an actuator which free end incorporates a loading sphere matching the loading depressions on the tibial models. The base of the press features a cylindrical loading cup used to secure the distal segment of the tibial models. To eliminate interference with the electromagnetic sensors, the press was built using non ferric material including brass, aluminum, PEEK and plexiglass.

Each model was rigidly coupled to the base of the press via a hollow fixture with corresponding dimensions (**Figure 4.7**). Specimens were then manually and non-destructively loaded for five cycles. A first cycle load of 200 N, used to allow the system to settle, was followed by four consecutive loads at 400 N each. Considering that each hind limb peak vertical force for a dog at the trot (~2 m/sec) is approximately 80% of its body weight, 400 N corresponds to 1.6 times (twice) the load placed on each hindlimb by a 25 kg dog as selected for in this study. This load was selected to represent a worse-case scenario mimicking lack of client compliance.

The procedure for loading weights was as follows:

- Cycle 1
    - First reading – no load to mark the baseline of the electromagnetic sensor locations in the environment
    - Second reading – manual loading to 200 N followed by data recording of electromagnetic sensors
- Cycles 2-5
    - Unloading occurred within 3-5 seconds of completion of the previous cycle and the first reading of the subsequent cycle was performed as described above
    - Second reading performed after manual loading to 400 N

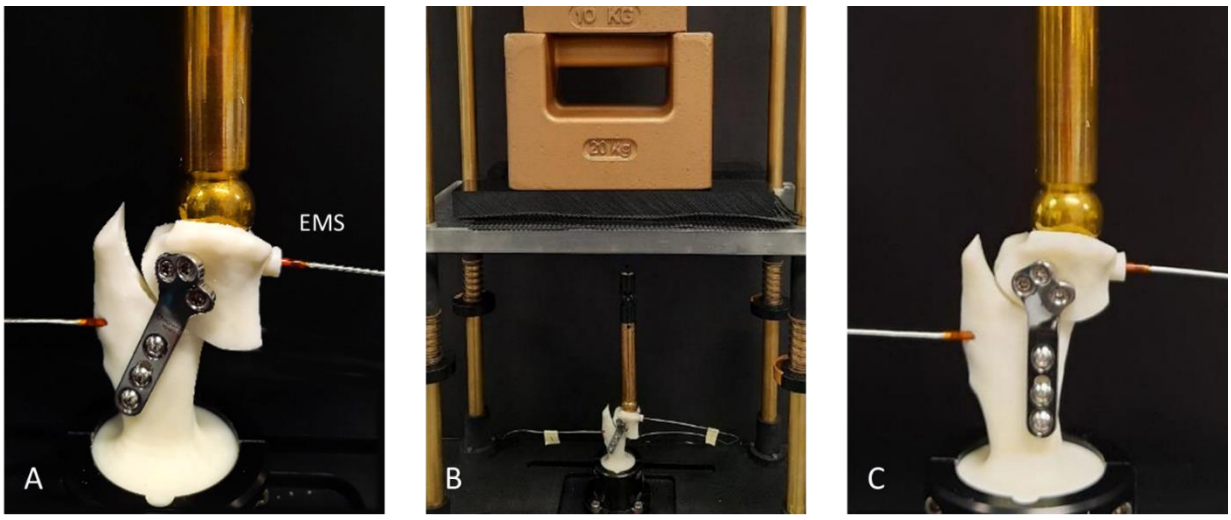

Figure 4.7. Specimens mounted into custom-built loading press

A – A downhill osteotomy with an inclined plate model is loaded into the press. A sensor is fixed within the tibial plateau segment and distal tibial segment. Note the increased osteotomy gap width secondary to rock-back. **B** – Wide view of the custom-built loading press with a mounted specimen during loading. **C** – A second specimen with an uphill osteotomy and straight plate orientation, is mounted into the frame for loading. Note the consistent width of the osteotomy gap.

Angular displacements about the X (craniocaudal – valgus/varus), Y (mediolateral – rock-back) and Z (proximodistal – internal/external rotation) axes were recorded. These values corresponded to roll, pitch and yaw, respectively. Whether contact occurred between segments and/or any failure (i.e., specimen breakage or screw pull-out) was recorded for all samples.

A Completely Randomized Design (CRD) was carried out to study the effect of plate inclination and osteotomy orientation on rock-back, roll and internal/external rotation. Mean values between the six groups were compared using a two-factor ANOVA and Tukey's post-hoc pairwise comparison when significance was found ($p<0.05$). When testing for interaction between plate inclination and osteotomy orientation, no significant interaction was found for any axis. Thus, the effect of plate inclination and osteotomy orientation on rock-back was analyzed independently.

Results

Data were normally distributed and satisfied the requirements of ANOVA. Within each osteotomy group, rock-back was significantly larger with inclined plates as compared to straight plates (p = 0) (**Figure 4.8**). Mean rock-back ± standard deviation for inclined plates compared to straight plates was 3.35° ± 0.33° and 2.01° ± 0.30°, respectively (**Table 1.1**). The difference between the two plate inclinations had a mean of 1.34° ± 0.40°. Osteotomy orientation had no significant effect on rock-back regardless of plate inclination (p = 0.105) (**Figure 4.9**). Mean rock-back ± standard deviation for uphill, normal and downhill osteotomies was 2.82° ± 0.59°, 2.55° ± 0.74° and 2.67° ± 0.86°, respectively (**Table 1.1**).

Conversely, plate inclination had no effect on roll (i.e. medio-lateral angulation) (p = 0.70), with the mean roll for inclined and straight pate groups being 3.91° ± 0.37° and 3.97° ± 0.43°, respectively (**Figure 4.10**). Similarly, osteotomy orientation had no effect on roll (p = 0.90) (**Figure 4.11**). Mean roll for uphill, normal and downhill osteotomies was 3.95° ± 0.34°, 3.98° ± 0.43° and 3.90° ± 0.42°, respectively (**Table 1.2**).

There was no effect of plate inclination or osteotomy orientation internal – external rotation (**Figures 4.12 and 4.13)**. The mean rotation for inclined and straight plate groups was 0.10° ± 0.29° and 0.51° ± 0.17°, respectively. The mean rotation for uphill, normal and downhill osteotomies was 0.40° ± 0.20°, 0.39° ± 0.29° and 0.12° ± 0.36°, respectively (**Table 1.3**).

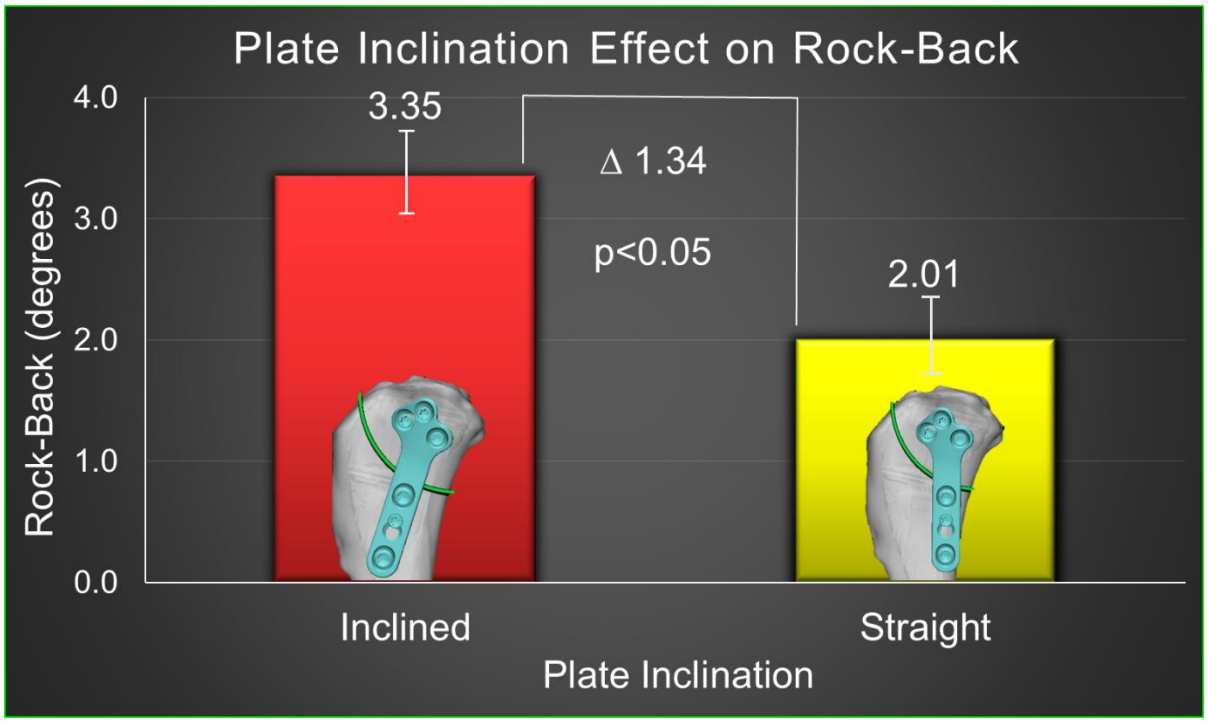

Figure 4.8. Histogram illustrating the effect of plate inclination on rock-back

The inclined plate group has a significantly (p = 0) larger rock-back mean (3.35°) than the straight plate group (2.01°).

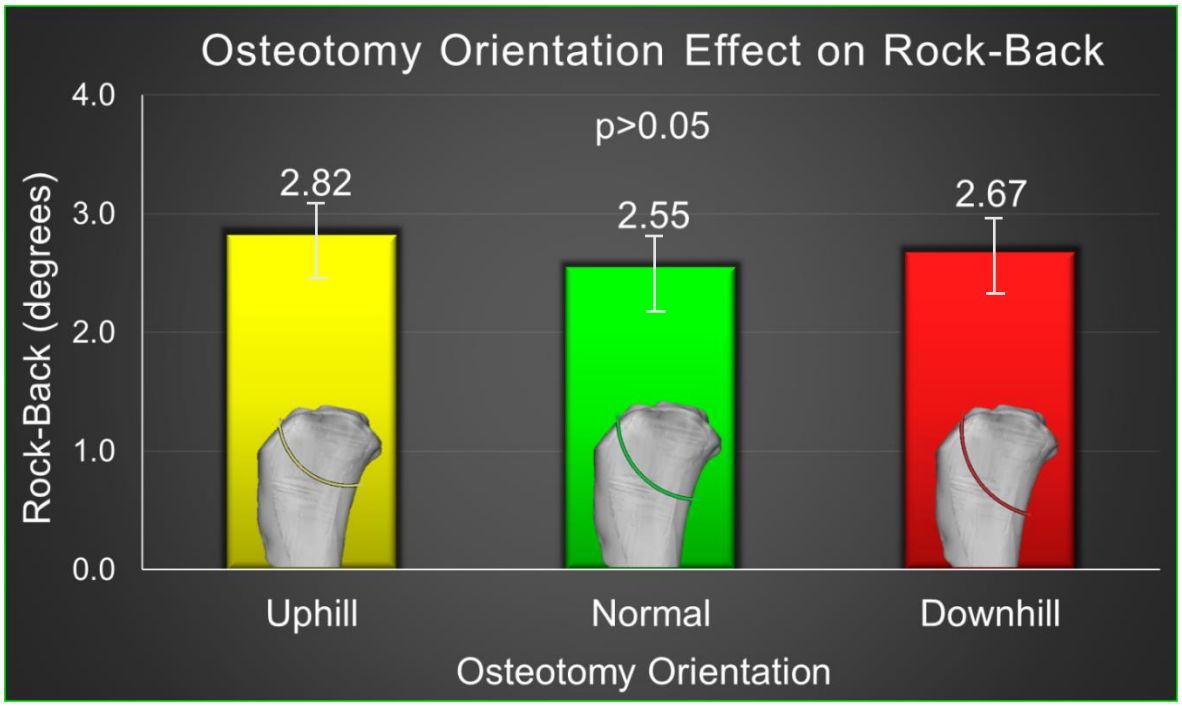

Figure 4.9. Histogram illustrating the effect of osteotomy orientation on rock-back

No significant difference was found between uphill, normal, and downhill osteotomy orientations on rock-back ($p>0.05$).

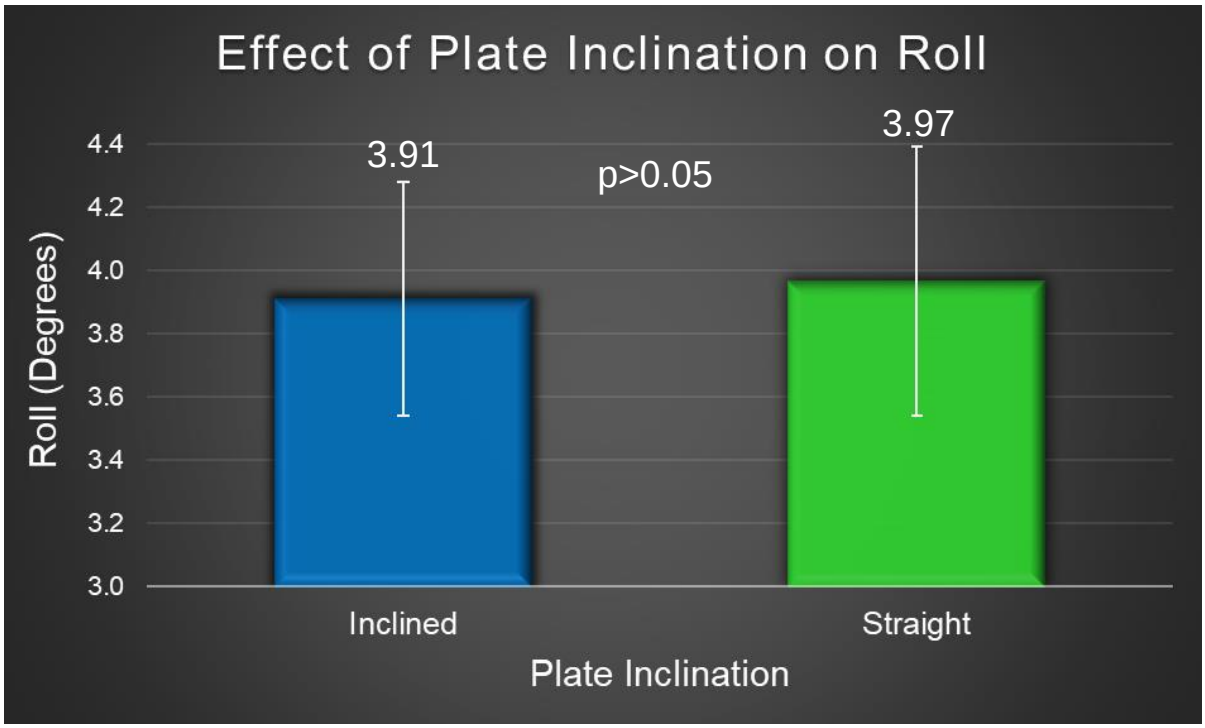

Figure 4.10. Histogram illustrating the effect of plate inclination on roll

No significant difference was found between straight and inclined plates on roll (p>0.05).

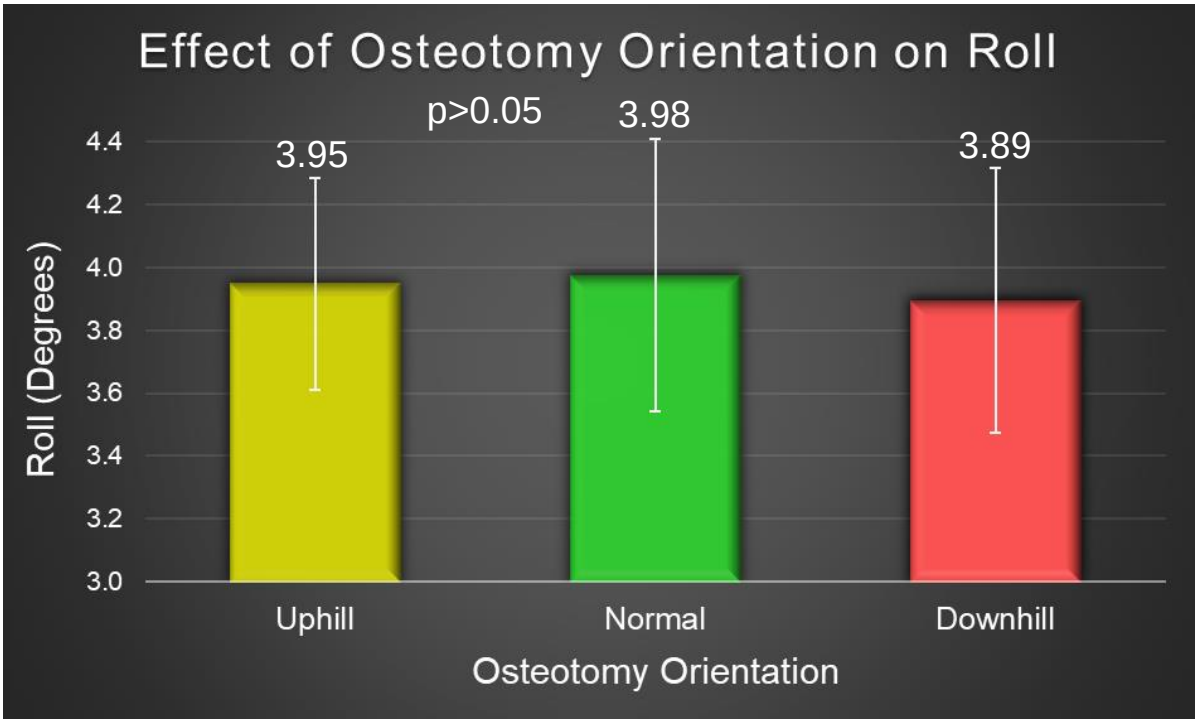

Figure 4.11. Histogram illustrating the effect of osteotomy orientation on roll

No significant difference was found between uphill, normal or downhill osteotomy orientations on roll ($p>0.05$).

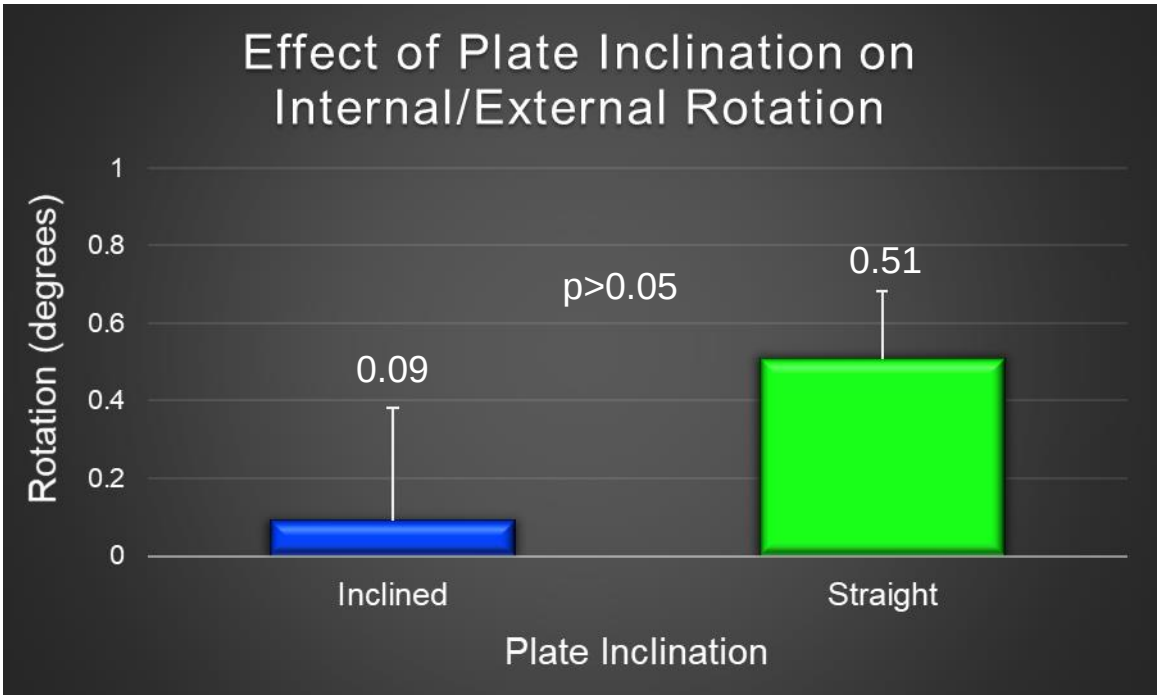

Figure 4.12. Histogram illustrating the effect of plate inclination on internal/external rotation

No significant difference was found between inclined and straight plates on rotation ($p>0.05$).

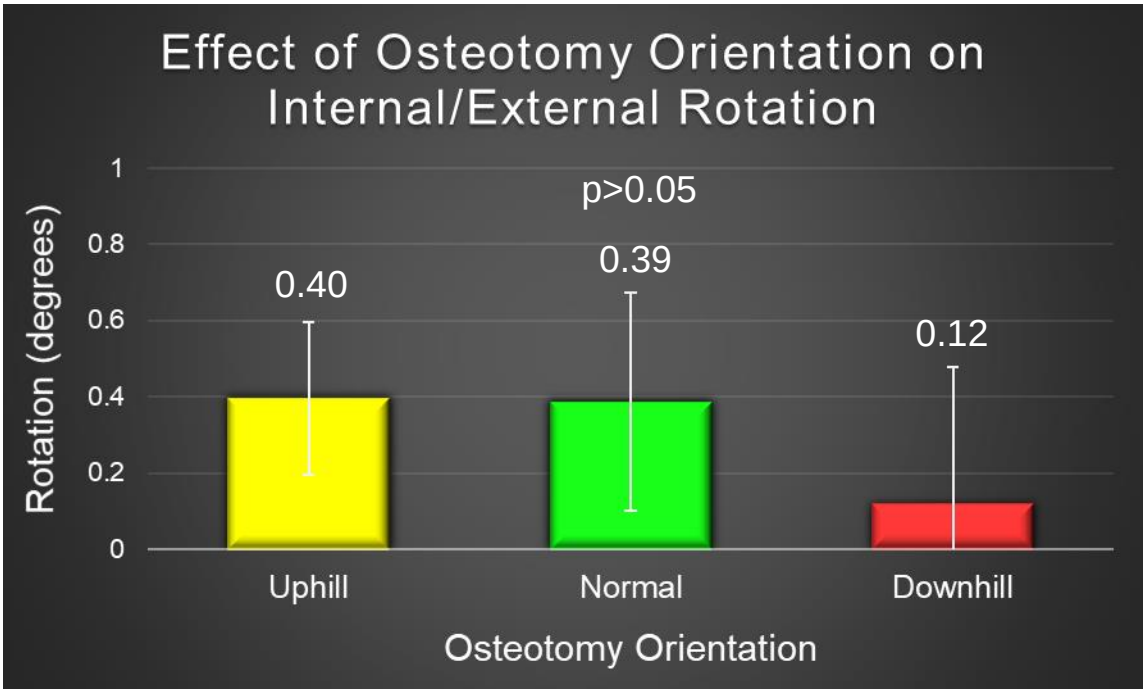

Figure 4.13. Histogram illustrating the effect of osteotomy orientation on internal/external rotation

No significant difference was found between uphill, normal or downhill osteotomy orientations on rotation ($p>0.05$).

Rock-Back (deg)	Mean	SD
Plate		
Inclined	3.352	0.344
Straight	2.007	0.298
Osteotomy		
Uphill	2.821	0.592
Normal	2.547	0.739
Downhill	2.672	0.856

Table 4.1. Illustration of rock-back for each plate inclination and osteotomy orientation

The mean and standard deviations for each group are shown in degrees.

Roll (deg)	Mean	SD
Plate		
Inclined	3.912	0.37
Straight	3.967	0.427
Osteotomy		
Uphill	3.948	0.337
Normal	3.975	0.433
Downhill	3.895	0.421

Table 4.2. Illustration of roll for each plate inclination and osteotomy orientation

The mean and standard deviations for each group are shown in degrees.

Rotation (deg)	Mean	SD
Plate		
Inclined	0.093	0.29
Straight	0.509	0.173
Osteotomy		
Uphill	0.396	0.201
Normal	0.386	0.286
Downhill	0.119	0.359

Table 4.3. Illustration of internal/external rotation for each plate inclination and osteotomy orientation

The mean and standard deviations for each group are shown in degrees.

Discussion

This study provides evidence to support the hypothesis that rock-back is amplified with a plate placed at an inclination to the caudal tibial cortex, and thus the tibial mechanical axis. On the contrary, osteotomy orientation has less of an effect on rock-back in this TPLO gap model.

Rock-back is defined as loss of reduction of tibial segments following TPLO. Previous reports in the literature have briefly suggested the occurrence of rock-back when assessing TPLO complications[1,17]. In other studies, effects of rock-back such as tibia/fibular fracture and implant failure have been observed, albeit no causative factors have been recognized and clinical significance has yet to be elucidated[30,42]. In one retrospective study, a mean change in TPA of 1.5° was noted at a mean follow-up of 6.5 weeks[38]. Although there was no effect of patient weight, plate type or osteotomy healing on rock-back, this difference was statistically significant. When assessing risk factors for fibular fracture after TPLO, a significant TPA difference of 5° between immediate post-operative and recheck radiographs was found in dogs that had sustained a fibular fracture as compared to 1.8° in dogs that had not[42]. An increase in post-operative TPA of 1.6° has also been significantly associated with bilateral, single-session TPLO and in dogs <15 kg with a high initial TPA of greater than 30°[43]. Although there has been no proven association with rock-back, locking TPLO plates have been shown to reduce overall complication rates and improve osteotomy healing over non-locking plates placed in the tibial plateau segment[44,45]. In one study, the mean post-operative TPA change was 1.9° with a significantly greater TPA change for non-locking over locking screws (2.59° vs. 1.29° respectively)[39]. A second study supported these results and demonstrated

significantly greater tibial plateau rock-back for conventional screws over locking screws with an average difference of 3.3°[40]. A third study evaluating non-locking and locking constructs did not show a significant difference in post-operative TPA between the two groups but still noted an overall TPA increase of 2.3° post-operatively[41]. Our study aimed to concentrate on two significant components of TPLO technique, plate and osteotomy placement, to identify their influence on rock-back. These factors were chosen based on anecdotal case examples showing rock-back occurrence with inclined plates and downhill osteotomies.

Interestingly, the overall mean rock-back for specimens with an inclined plate was 3.35° as compared to 2.00° for the straight plate models. This demonstrates that rock-back occurs after TPLO in an experimental setting after only five cycles of loading and is similar to the magnitude of rock-back described in previous studies[39-41]. When extrapolating this to a clinical scenario, one can speculate that rock-back magnitude may further increase during the first postoperative weeks preceding clinical union as cyclical loading occurs. Retrospective studies are warranted to assess the clinical relevance of the amount of rock-back that occurs during the postoperative bone healing period.

When evaluating the influence of osteotomy orientation on rock-back, no significant differences were found. Our study used a gap model reproducing a clinical scenario where interfragmentary compression has not been achieved. In our study, although reduction in gap size occurred during loading, absence of contact between the tibial segments was observed in all models. This likely mitigated the potential sliding of the tibial plateau resulting from a shear force at the osteotomy interface. Therefore, we surmise that with a contact model, a difference in rock-back based on osteotomy

orientation could be observed. Based on the results of our study, we conclude that with incomplete compression of the tibial segments during TPLO, osteotomy orientation has less of an influence on rock-back than plate inclination. Until further studies elucidate the effect of osteotomy on rock-back in a contact model, we recommend avoiding a downhill osteotomy based on the theory of increased shear forces at the interfragmentary interface.

Although the influence of the size of the osteotomy gap on rock-back was not evaluated in this study, it is not uncommon to observe incomplete compression during or after TPLO surgery. In this experiment, a gap model was chosen to replicate a worst-case scenario observed clinically. However, the presence of an osteotomy gap may itself induce motion of the tibial plateau segment and predispose to rock-back. In our study, the cranioproximal osteotomy gap was increased beyond 1 mm after loading in all specimens. We postulate that this cranial gap increase may lead to loss of buttress support for the tibial crest, thereby increasing the risk for tibial tuberosity fracture. Indeed, in a previous study evaluating risk factors for tibial tuberosity fracture following TPLO, a TPA change of 3.2° was found in dogs sustaining a tibial tuberosity fracture compared to 0.98° in dogs without this fracture complication. This supports the theory that the presence of an osteotomy gap may induce rock-back and subsequent bone failure in the form of tibial tuberosity fracture[30]. Future studies are warranted to evaluate the effect of the magnitude of an osteotomy gap and its association with tibial tuberosity fracture following post TPLO rock-back.

Although a smaller focus of our study, we were interested to learn whether roll or internal/external rotation were affected by rock-back. Roll was defined as the movement

of the tibial plateau segment in a medio-lateral direction about the X-axis. Our results showed that plate inclination and osteotomy orientation did not alter roll significantly. Nevertheless, it is important to note that roll in the direction of the lateral cortex was present in all models with a mean of 3.94°. While the impact of increased roll on TPLO outcome is unknown, one can speculate that increased roll contributes to fibular fracture and thus decrease in interfragmentary stability, which in turn could contribute to rock-back.

Similarly, internal/external rotation had no effect on rock-back in this study. Rotation was defined as displacement of the tibial plateau segment about the Z-axis, reflecting internal and external tibial plateau rotation. This finding was expected as shear forces should not dictate interfragmentary movement in this direction. The interaction of cortices of both tibial segments is at the same level throughout all interfragmentary contact points, thus minimizing shear forces in this direction.

Based on a comprehensive literature review, this is the first experimental study evaluating specific factors of rock-back following TPLO. Since the development of TPLO, a variety of surgical techniques have been suggested to optimize outcome, including the use of a jig to ensure appropriate alignment, pre-operative measurement techniques for saw blade placement[46-49] the use of locking screws in the proximal tibial segment[39,40,44], and centering of the osteotomy on the intercondylar tubercles of the tibia[14,50]. Here we propose that standardization of technique involves placement of the TPLO plate parallel to the caudal tibial cortex, and thus consequently, near parallel to the tibial mechanical axis. The caudal tibial cortex was chosen as the landmark in this study because it was easily identifiable on our models and can similarly be identified intra-operatively. There

was a 5° angle between the caudal tibial cortex and tibial mechanical axis as measured on the tibia in this study. This angle remains constant across all models. Thus, the 20° plate inclination relative to the caudal tibial cortex chosen in this study illustrated a worst-case scenario of plate placement approximately 15° relative to the tibial mechanical axis. Future studies should investigate the relationship between increasing plate inclination and rock-back magnitude. From a practical standpoint, it is feasible to inadvertently incline a TPLO plate when proximal tibial bone stock is limited. This may occur when choosing a smaller sized saw blade, or when selecting a larger bone plate to compensate for an increased BCS.

One of our goals was to provide objective data regarding optimal plate placement during TPLO. Residents, early-career surgeons and other trainees studying the TPLO technique may be less inclined to place emphasis on plate orientation and alternatively focus on ensuring the proximal screws engage adequate bone without joint or osteotomy involvement. Inclining the TPLO plate facilitates screw insertion into the tibial plateau avoiding the cranial aspect of the osteotomy, particularly in small tibial plateau segments. It also limits the risk of iatrogenic damage to the caudal tibial cortex if a plate is inadvertently positioned too caudally. With proper visualization and instrument-guided palpation of the caudal tibial cortex during surgery, placement of the bone plate parallel to this cortex, and thus relatively parallel to the tibial mechanical axis, should be readily achievable.

Our study did not confirm the second hypothesis in that a downhill osteotomy induces a larger rock-back secondary to greater shear force between tibial segments. Considering that 1) the difference in rock-back between osteotomy orientation was of a

similar magnitude as that observed with plate inclination, 2) the lack of a contact model prevented continuous compression between tibial segments and 3) that the small sample size may have resulted in a type 2 statistical error, our recommendation is to avoid an excessive downhill cut until further studies elucidate the effect of osteotomy using a contact model.

It is currently unknown whether the degree of rock-back observed in our study induces clinically relevant stifle instability. For clinical cases in which the TPLO bone plate is positioned at an excessive incline to the caudal tibial cortex, we recommend close follow-up with increased exercise restriction and urge consideration of repeat radiographs sooner than the traditional post-operative period of 6-8 weeks. Rock-back can be clinically monitored with sequential measurements of TPA, using the immediate post-operative TPA as a reference point. Revision surgery should only be considered after evaluating all aspects of clinical signs, orthopedic examination, and evidence of subsequent rock-back complications such as fibular, tibial, or implant failure in an individual patient. However, revision surgery may be challenging due to the diminished bone stock available for fixation associated with the original screw holes.

This study focused on 3D rendered tibial bone models which allowed for standardization across groups and eliminated the inherent variability of using cadaveric specimens. Although the resin material did not have the exact characteristics of bone, each group acted as its own control. Utilizing 3D designed models is gaining popularity in veterinary medicine particularly with the use of patients-specific surgical guides[2,3,4]. Here we describe its innovative role in veterinary biomechanical research. We demonstrated feasibility and success with using 3D printed models to create a TPLO

simulation within a loading frame. This model may be applied to different 3D printed bones in the dog to test loading in a controlled setting across a variety of long bones and joints.

To the authors' knowledge, an electromagnetic tracking system has not been utilized to study motion of a veterinary bone construct prior to this study. This system utilizes technology that is reliable and accurate on a microscale. Small sensors placed on or within bone models are readily recognized by the field generator's magnetic field, eliminating the necessity of direct line-of-sight transmission that optical tracking systems require[8,10]. Electromagnetic tracking systems have been successfully tested with human robotics, tracing of surgical instruments in minimally invasive procedures, and radiotherapy, with expansion of this utility in veterinary medicine research as supported by our study[8,10].

Limitations of this research include lack of a retrospective study to translate experimental rock-back into clinical outcome. The 3D printed models in this study did not mimic exact bone material properties of an *in vivo* canine tibia. However, all models were standardized as previously discussed, thus eliminating any external factors that may have impacted on rock-back outcome and permitting direct comparison between groups. In addition, the lack of a comparative contact model study precludes assumptions regarding osteotomy orientation on rock-back. Nonetheless, the results of this research support a strong influence of an inclined plate inducing a greater degree of rock-back.

In conclusion, we recommend refining and standardizing the TPLO surgical technique to include placement of the bone plate parallel to the tibial mechanical axis to

reduce the risk of rock-back and its sequelae. This will in turn enhance resident and surgeon training and promote consistency of the TPLO procedure.

APPENDIX

Design of a Custom-Built Loading Press

All of the following was designed with SolidWorks CAD software and all units are in inches

1. **Base Plate – Figure 4.14**
    a. Create rectangular plate with dimensions:
        i. Length = 15.93
        ii. Width = 7.78
        iii. Height = 1.00
    b. Main base plate contains 4 tapped holes:
        i. 1.00 from all edges of base
        ii. Diameter = 0.25
        iii. Through holes
    c. Create center rectangular depression to accept coupling base:
        i. Length = 5.00
        ii. Height = 3.00
        iii. Recess into main base plate by 0.25
        iv. Fillet edges with radius = 0.35
    d. Center base plate contains 4 tapped holes:
        i. 1/4 – 20 UNC screws
        ii. Through holes
        iii. All holes placed 7.10 from edge of main base plate (length)
        iv. All holes placed 3.03 from edge of main base plate (height)
        v. Distance between holes = 1.724
    e. Rectangular recess dimensions:

i. Length = 8.35

ii. Height = 0.50

iii. Recess into main base plate by 0.31

iv. Distance from top edge of main base plate = 1.57

2. <u>Base Coupling Fixture – Figure 4.15</u>

a. Fixture base dimensions:

i. Design a circle

1. Outer diameter = 2.875
2. Inner diameter (for centering of tapped holes) = 2.438
3. Height = 0.38

ii. Tapped holes x 4 equidistant along circular base

1. Diameter = 0.26
2. Through holes
3. Center of holes passes through inner diameter of fixture base

b. Coupling Cylinder

i. Dimensions:

1. Outer diameter = 2.00
2. Inner diameter = 1.50
3. Thickness of cylinder edge = 0.25
4. Height = 1.6

ii. Tapped holes x 4

1. Diameter = 0.14
2. Distance between hole centers = 1.75

3. Distance from distal hole center to bottom of base fixture = 0.675
4. Distance from proximal hole center to bottom of base fixture = 1.675
5. Distance from holes to edge of coupling cylinder = 0.30
6. Counterbore for 6-32 screw

iii. Front side of coupling cylinder should contain recession to accept model base

1. Radius = 0.12

3. <u>PEEK Frame (main base)</u>

a. Rectangular dimensions – no fillet:

i. Length = 15.93

ii. Width = 7.78

b. Tapped holes along frame corners x 4

i. Diameter = 0.75

ii. Distance from edge of plate = 1.00

iii. Through holes

c. Center hole to accept X-Bar:

i. Length = 11.00

ii. Width = 1.50

iii. Fillet corners with radius 0.10

d. Inner rectangle to accept coupling insert

i. Length = 12.00

ii. Width = 2.50

iii. Tapped holes equidistant x 10

1. Diameter = 0.14

4. <u>PEEK Frame (coupling insert)</u>

a. Rectangular dimensions – fillet radius 0.10:

i. Length = 12.00

ii. Width = 2.50

b. Tapped holes equidistant along frame x 10

i. Diameter = 0.15

ii. Coupling interface of 0.28 diameter on top (100°)

1. For flat head machine screw

c. Center hole to lock X-Bar:

i. Length = 10.00

ii. Width = 0.20

iii. Fillet?

5. <u>X-Bar (to couple with insert of PEEK frame) – Figure 4.16</u>

a. Bar dimensions:

i. Length = 10.00

ii. Width = 1.50

iii. Height = 1.10

b. Center elevated rectangle to couple with PEEK insert:

i. Length = 10.00

ii. Width = 0.20

iii. Height = 0.10

c. Tapped holes to accept PEEK insert:

i. Diameter = 0.14 (for PEEK)

ii. Diameter = 0.11 (for Y-Bar)

iii. Through holes

iv. 3.00 from either edge (4.00 distance apart)

d. Extrusion x 2 to accept Y-Bar:

i. Length = 0.25

ii. Width of extrusion = 1.5 (entire width of bar)

iii. No fillet

iv. Recession to depth of 0.25

v. Distance from bar edges = 2.00

6. <u>Y-Bar (to couple with X-Bar) – Figure 4.17</u>

a. Bar dimensions:

i. Length = 10.000

ii. Width = 1.50

iii. Height = 0.60

b. Extruded rectangles x 2 to couple with X-Bar

i. Length = 0.25

ii. Width = 1.5

iii. No fillet

iv. Elevate to 0.20

v. Distance from bar edges = 2.00

c. Bottom extrusion to accept universal joint
    i. Length = 1.5
    ii. Width = 1.5
    iii. Height = 1.00
    iv. Centered hole with diameter of 0.69 and distance of 0.80
    v. Tapped hole on one side of extrusion with diameter of 0.25 and tapped distance of 0.41
d. Holes on main Y-Bar to lock into X-Bar:
    i. Width = 1.20
        1. Fillet with radius 0.10 on either end
    ii. Distance from bar edges = 3.00

7. <u>Additional pieces purchased to assemble press (McMaster Carr):</u>

a. Quick-release clamping shaft collar x 4 (1511K210)
    i. OD = 2
    ii. ID = 0.75
    iii. Width = 0.5
b. Single universal joint (60625K870)
    i. For shaft diameter 3/8
    ii. For shaft depth 7/8
    iii. Joint diameter = 11/16
    iv. Overall length = 2.66
    v. Maximum operating angle = 45°
c. Steel socket head screw for universal joint (91251A148)

i. Screw OD = 0.138

ii. Head diameter = 0.226

iii. Screw length = 0.5

d. Thumb screws for locking the translational bars to the press (93585A015, 93585A016)

i. Thread OD = 0.138

ii. Screw lengths = 0.75, 0.5

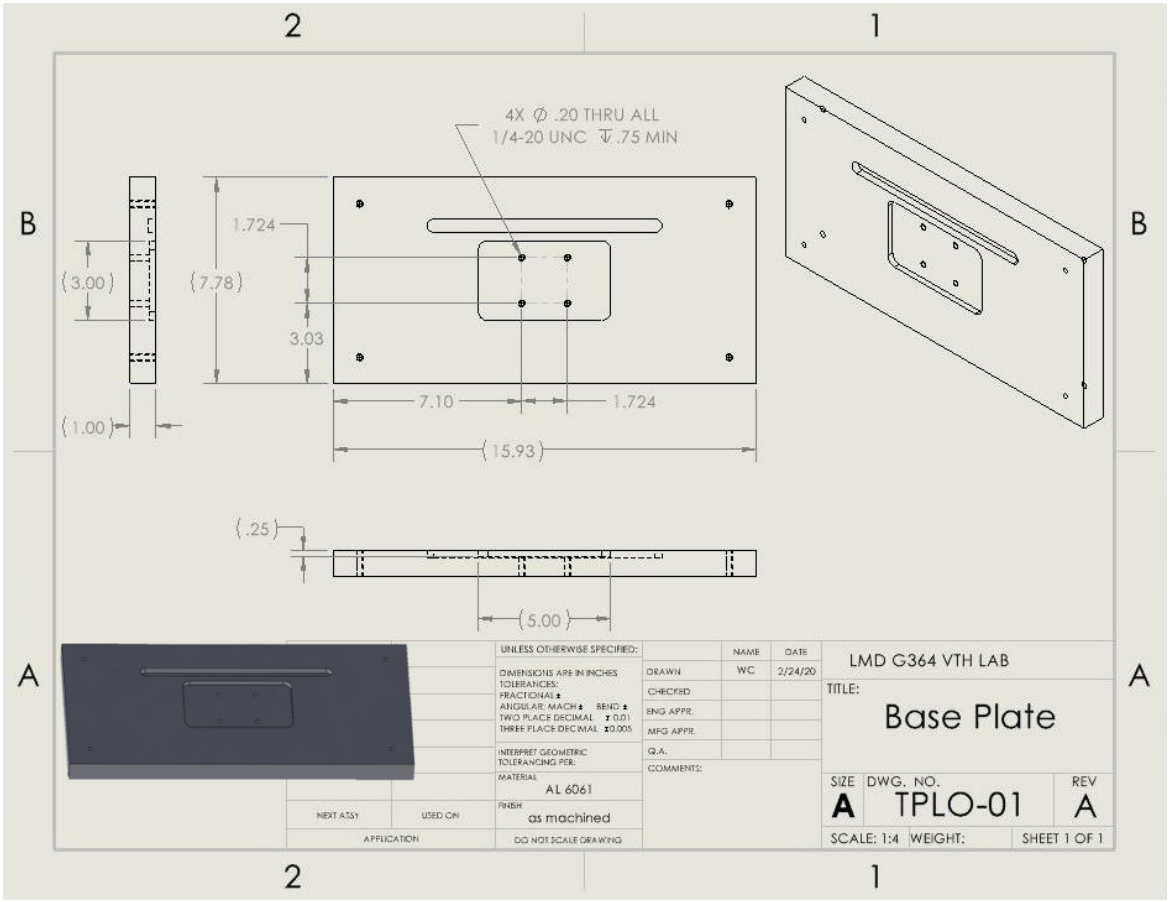

Figure 4.14. CAD drawing of the base plate of the custom-built loading press

This base plate will be assembled to the base fixture shown in Figure 4.1.

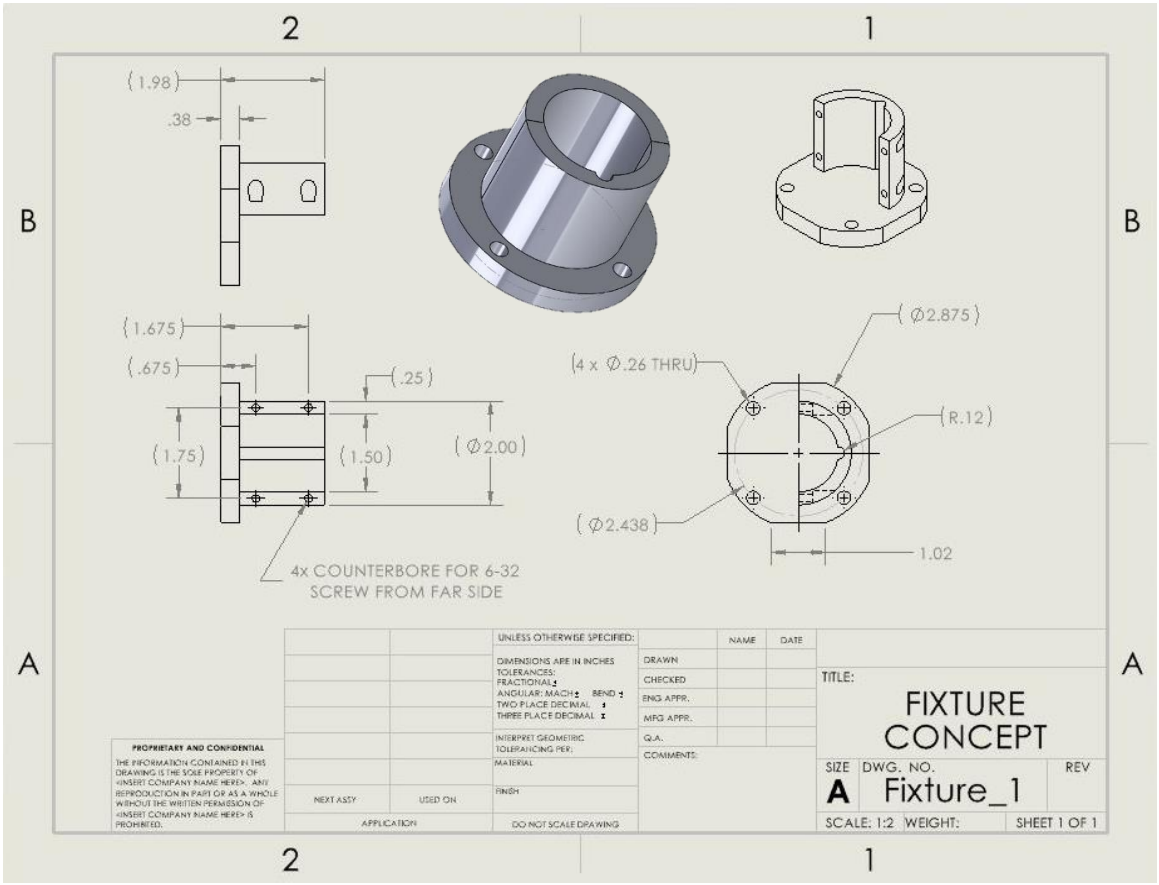

Figure 4.15. CAD drawing of the base fixture coupled to the base plate of the custom-built loading press

The two hemi-cylindrical components are separately designed and then assembled to ensure a press-fit locking system for each specimen.

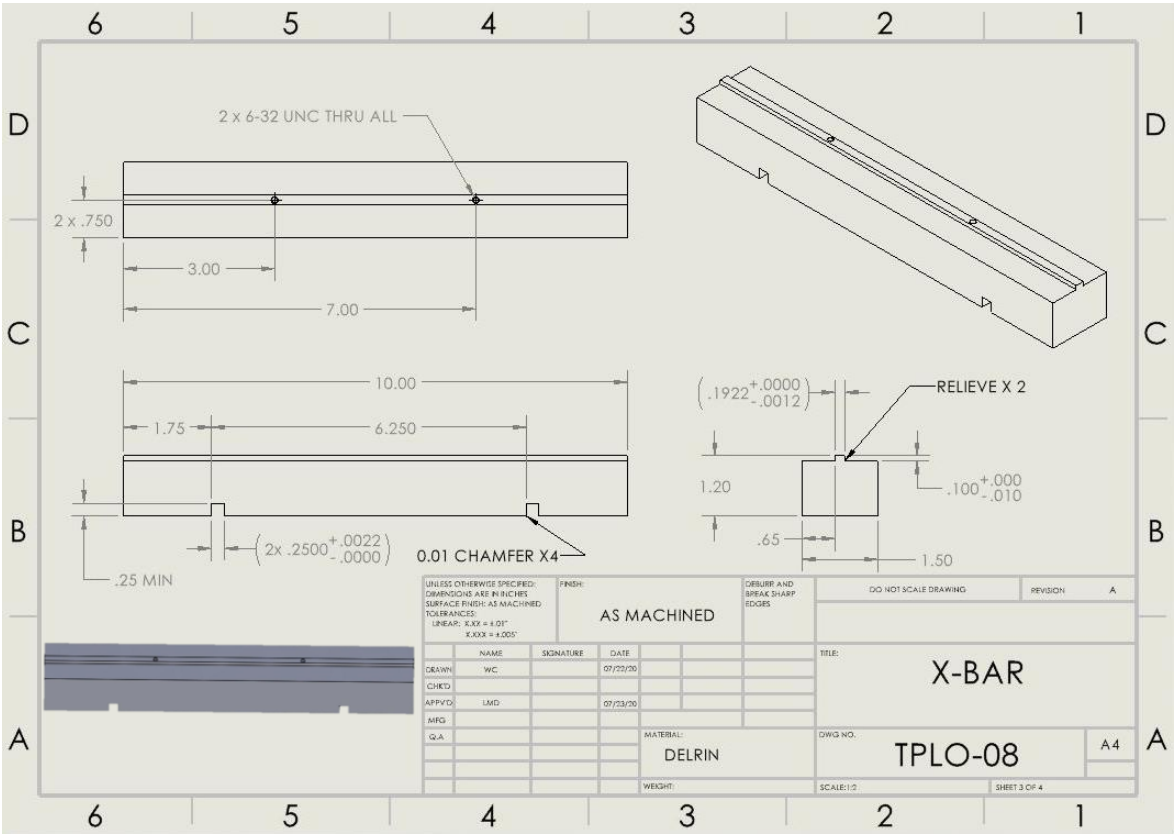

Figure 4.16. CAD drawing of X-Bar of the custom-built loading press for translation along the craniocaudal axis

This is coupled to both the PEEK loading frame and Y-Bar as shown in the assembly of Figure 4.5.

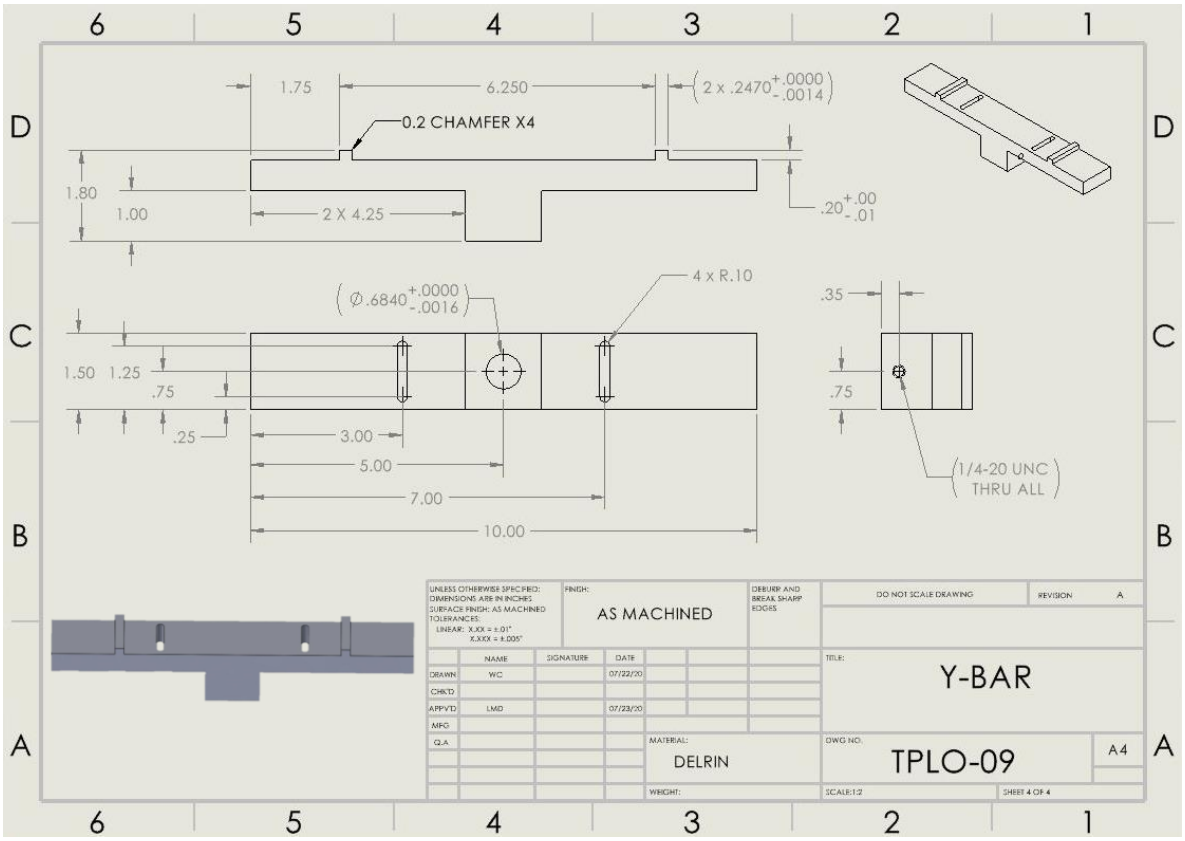

Figure 4.17. CAD drawing of the Y-Bar of the custom-built loading press for translation along the mediolateral axis

This is coupled to the X-Bar and the universal joint containing the loading sphere.

REFERENCES

REFERENCES

1. Kloc P, Kowaleski MP, Litsky AS, Brown NO, Johnson KA. Biomechanical Comparison of Two Alternative Tibial Plateau Leveling Osteotomy Plates with the Original Standard in an Axially Loaded Gap Model: An In Vitro Study. *Vet Surg*. 2009;38(1):40-48.

2. Easter TG, Bilmont A, Pink J, Oxley B. Accuracy of three-dimensional printed patient-specific drill guides for treatment of canine humeral intracondylar fissure. *Vet Surg*. 2020;49(2):363-372.

3. Toni C, Oxley B, Behr S. Atlanto-axial ventral stabilisation using 3D-printed patient-specific drill marturelloguides for placement of bicortical screws in dogs. *J Small Anim Pract*. 2020;61(10):609-616.

4. Hall EL, Baines S, Bilmont A, Oxley B. Accuracy of patient-specific three-dimensional-printed osteotomy and reduction guides for distal femoral osteotomy in dogs with medial patella luxation. *Vet Surg*. 2019;48(4):584-591.

5. Marturello DM, Wei F, Déjardin LM. Characterization of the torsional structural properties of feline femurs and surrogate bone models for mechanical testing of orthopedic implants. *Vet Surg*. 2019;48(2):29-236.

6. Moeller EM, Cross AR, Rapoff AJ. Change in Tibial Plateau Angle After Tibial Plateau Leveling Osteotomy in Dogs. *Vet Surg*. 2006;35(5):460-464.

7. Merriaux P, Dupuis Y, Boutteau R, Vasseur P, Savatier X. A Study of Vicon System Positioning Performance. *Sensors*. 2017;17(7):1591.

8. Sorriento A, Porfido MB, Mazzoleni S, et al. Optical and Electromagnetic Tracking Systems for Biomedical Applications: A Critical Review on Potentialities and Limitations. *IEEE Rev Biomed Eng*. 2020;13:212-232.

9. Wynn W, Frahm C, Carroll P, Clark R, Wellhoner J, Wynn M. Advanced superconducting gradiometer/Magnetometer arrays and a novel signal processing technique. *IEEE T Magn*. 1975;11(2):701-707.

10. Franz AM, Haidegger T, Birkfellner W, Cleary K, Peters TM, Maier-Hein L. Electromagnetic Tracking in Medicine—A Review of Technology, Validation, and Applications. *IEEE Trans Med Imaging*. 2014;33(8):1702-1725.

11. AZoM. Stainless Steel - Grade 316L - Properties, Fabrication and Applications (UNS S31603). *AZoM website*. 2004. Accessed March 20, 2021. www.azom.com/article.aspx?ArticleID=2382.

12. Dismukes DI, Tomlinson JL, Fox DB, Cook JL, Witsberger TH. Radiographic Measurement of Canine Tibial Angles in the Sagittal Plane. *Vet Surg*. 2008;37(3):300-305.
13. Kowaleski MP, Boudrieau RJ, Pozzi A. Chapter 62: Stifle Joint. In: Johnston SA, Tobias KM, eds. Veterinary Surgery: Small Animal. 2nd ed. Elsevier; 2018:906-998.

14. Warzee CC, Dejardin L]c, Arnoczky SP, Perry RL. Effect of tibial plateau leveling on cranial and caudal tibial thrusts in canine cranial cruciate deficient stifles: An in vitro experimental study. *Vet Surg*. 2001;30(3):278-286.

15. Sherman MA, Seth A, Delp SL. What is a Moment Arm? Calculating Muscle Effectiveness in Biomechanical Models Using Generalized Coordinates. *Proc ASME Des Eng Tech Conf*. 2013;7(B):1-18.

16. Hayashi K, Manley PA, Muir P. Cranial Cruciate Ligament Pathophysiology in Dogs with Cruciate Disease: A Review. *J Am Anim Hosp Assoc.* 2004;40:385-390.

17. Kim, SE. Pozzi A. Kowaleski MP. Lewis DD. Tibial Osteotomies for Cranial Cruciate Ligament Insufficiency in Dogs. *Vet Surg*. 2008;37(2):111-125.

18. Niebauer GW, Wolf B, Bashey RI, Newton CD. Antibodies to Canine Collagen Types I and II in Dogs with Spontaneous Cruciate Ligament Rupture and Osteoarthritis. *Arthritis and Rheumatism.* 1987;30(3):319-327.

19. Arnoczky SP, Warren RF, Minei JP. Replacement of the anterior cruciate ligament using a synthetic prosthesis. *Am J Sports Med*. 1986;14(1):1-6.

20. Slocum B, Slocum TD. Tibial plateau leveling osteotomy for repair of cranial cruciate ligament rupture in the canine. *Vet Clin North Am Small Anim Pract.* 1993; 23(4): 777-795.

21. DeCamp CE, Johnston SA, Dejardin LM, Schaefer SL. Brinker, Piermattei, and Flo's Handbook of Small Animal Orthopedics and Fracture Repair. 5th ed. Elsevier; 2016.

22. Dejardin LM. Chapter 148: Tibial Plateau Leveling Osteotomy. In: Slatter D. *Textbook of Small Animal Surgery.* 3rd ed. Volume 2. Elsevier; 2003:2133-2143.

23. Shahar R, Milgram J. Biomechanics of Tibial Plateau Leveling of the Canine Cruciate-Deficient Stifle Joint: A Theoretical Model. *Vet Surg*. 2006;35(2):144-149.

24. Barnes DC, Trinterud T, Owen MR, Bush MA. Short-term outcome and complications of TPLO using anatomically contoured locking compression plates in small/medium-breed dogs with "excessive" tibial plateau angle. *J Small Anim Pract*. 2016; 57(6): 305-310

25. Stauffer KD, Tuttle TA, Elkins AD, Wehrenberg AP, Character BJ. Complications Associated With 696 Tibial Plateau Leveling Osteotomies (2001–2003). *J Am Anim Hosp Assoc*. 2006;42(1):44-50.
26. Gatineau M, Dupuis J, Planté J, Moreau M. Retrospective study of 476 tibial plateau levelling osteotomy procedures. *Vet Comp Orthop Traumatol*. 2011;24(05):333-341.

27. Bergh MS, Peirone B. Complications of tibial plateau levelling osteotomy in dogs. *Vet Comp Orthop Traumatol*. 2012;25(05):349-358.

28. Coletti TJ, Anderson M, Gorse Mary Jean, Madsen R. Complications associated with tibial plateau leveling osteotomy: A retrospective of 1519 procedures. *Can Vet J* 2014;55(3):249–254.

29. Pacchiana PD, Morris E, Gillings SL, Jessen CR, Lipowitz AJ. Surgical and postoperative complications associated with tibial plateau leveling osteotomy in dogs with cranial cruciate ligament rupture: 397 cases (1998-2001). *J Am Vet Med Assoc.* 2003;222(2):184-193.

30. Bergh MS, Rajala-Schultz P, Johnson KA. Risk Factors for Tibial Tuberosity Fracture After Tibial Plateau Leveling Osteotomy in Dogs. *Vet Surg*. 2008;37(4):374-382.

31. Solano MA, Danielski A, Kovach K, Fitzpatrick N, Farrell M. Locking Plate and Screw Fixation After Tibial Plateau Leveling Osteotomy Reduces Postoperative Infection Rate in Dogs Over 50 kgcol. *Vet Surg*. 2015;44(1):59-64.

32. Kergosien DH, Barnhart MD, Kees CE, et al. Radiographic and Clinical Changes of the Tibial Tuberosity after Tibial Plateau Leveling Osteotomy. *Vet Surg*. 2004;33(5):468-474.

33. Hans E, Barnhart M, Kennedy S, Naber S,. Comparison of complications following tibial tuberosity advancement and tibial plateau levelling osteotomy in very large and giant dogs 50 kg or more in body weight. *Vet Comp Orthop Traumatol*. 2017;30(04):299-305.

34. Tuttle T, Manley P. Risk Factors Associated with Fibular Fracture After Tibial Plateau Leveling Osteotomy. *Vet Surg*. 2009;38(3):355-360.

35. Collins JE, Degner DA, Hauptman JG, DeCamp CE. Benefits of Pre- and Intraoperative Planning for Tibial Plateau Leveling Osteotomy. *Vet Surg*. 2014;43(2):142-149.

36. Boekhout C, Cross A. Incidence of Transcortical Tibial Fractures with Self-Tapping and Non-Self-Tapping Screws in a Canine TPLO Model. *Vet Surg*. 2012;41(7):898-901.

37. Pozzi A, Dunbar NJ, Kim SE. Effect of tibial plateau leveling osteotomy on patellofemoral alignment: A study using canine cadavers. *Vet J*. 2013;198(1):98-102.
38. Moeller EM, Allen DA, Wilson ER, Lineberger JA, Lehenbauer T. Long-term outcomes of thigh circumference, stifle range-of-motion, and lameness after unilateral tibial plateau levelling osteotomy. *Vet Comp Orthop Traumatol*. 2010;23(01):37-42.

39. Conkling AL, Fagin B, Daye RM. Comparison of Tibial Plateau Angle Changes after Tibial Plateau Leveling Osteotomy Fixation with Conventional or Locking Screw Technology. *Vet Surg*. 2010;39(4):475-481.

40. Leitner M, Pearce SG, Windolf M, Schwieger K, Zeiter S, Schawalder P et al. Comparison of Locking and Conventional Screws for Maintenance of Tibial Plateau Positioning and Biomechanical Stability After Locking Tibial Plateau Leveling Osteotomy Plate Fixation. *Vet Surg*. 2008;37(4):357-365.

41. Krotscheck U, Thompson MS, Ryan KK, Mohammed HO. Comparison of Tibial PA, Bone Healing, and Intra-articular Screw Placement using Conventional Nonlocked Application of Surgeon-Contoured versus Locked Application of Precontoured TPLO Plates in Dogs. *Vet Surg*. 2012;41(8):931-937.

42. Taylor J, Langenbach A, Marcellin-Little DJ. Risk Factors for Fibular Fracture after TPLO. *Vet Surg*. 2011;40(6):687-693.

43. Witte PG, Scott HW. Tibial Plateau Leveling Osteotomy in Small Breed Dogs With High Tibial Plateau Angles Using a 4-Hole 1.9/2.5 mm Locking T-Plate. *Vet Surg*. 2014;43(5):549-557.

44. Kowaleski MP, Boudrieau RJ, Beale BS, Piras A, Hulse D, Johnson KA. Radiographic outcome and complications of tibial plateau leveling osteotomy stabilized with an anatomically contoured locking bone plate. *Vet Surg*. 2013.

45. Bordelon J, Coker D, Payton M, Rochat M. An in vitro mechanical comparison of tibial plateau levelling osteotomy plates. *Vet Comp Orthop Traumatol*. 2009;22(06):467-472.

46. Restle KN, Biskup JJ. A novel jig arm to measure tibial plateau angle during tibial plateau leveling osteotomy. *Vet Surg*. 2017;46(7):1032-1038.

47. Burton NJ, Fitzpatrick N, Wallace AM. Evaluation of Cut Accuracy and Cis Cortical Damage for Tibial Plateau Leveling Osteotomy Performed with and without Aid of a Novel Saw Guide: An In Vitro Study. *Vet Surg*. 2013;42(1):28-37.

48. Mariano AD, Kowaleski MP, Boudrieau RJ. Novel TPLO Alignment Jig/Saw Guide Reproduces Freehand and Ideal Osteotomy Positions. *PLOS ONE*. 2016;11(8):1-15.

49. Mossman H, Nicholson M, Phelps H, et al. Accuracy of three pre- and intraoperative measurement techniques for osteotomy positioning in the tibial plateau levelling procedure. *Vet Comp Orthop Traumatol*. 2015;28(04):250-255.
50. Kowaleski MP, Apelt D, Mattoon JS, Litsky AS. The Effect of Tibial Plateau Leveling Osteotomy Position on Cranial Tibial Subluxation: An In Vitro Study. *Vet Surg*. 2005;34(4):332-336.

51. Robinson DA, Mason DR, Evans R, Conzemius. The Effect of Tibial Plateau Angle on Ground Reaction Forces 4-17 Months After Tibial Plateau Leveling Osteotomy in Labrador Retrievers. *Vet Surg*. 2006;35(3):294-299.

52. Ballagas AJ, Montgomery RD, Henderson RA, Gillette R. Pre- and Postoperative Force Plate Analysis of Dogs with Experimentally Transected Cranial Cruciate Ligaments Treated Using Tibial Plateau Leveling Osteotomy. *Vet Surg*. 2004;33(2):187-190.

53. Kim SE, Lewis DD, Pozzi A. Effect of Tibial Plateau Leveling Osteotomy on Femorotibial Subluxation: In Vivo Analysis during Standing. *Vet Surg*. 2012;41(4):465-470.

54. Castilho M, Dias M, Vorndran E, et al. Application of a 3D printed customized implant for canine cruciate ligament treatment by tibial tuberosity advancement. *Biofabrication*. 2014;6(2):1-13.

55. Woodbridge N, Corr SA, Grierson J, Arthurs G. A retrospective study of tibial plateau translation following tibial plateau levelling osteotomy stabilisation using three different plate types. *Vet Comp Orthop Traumatol*. 2011;24(06):445-449.

56. Brown NP, Bertocci GE, Marcellin-Little DJ. Canine stifle joint biomechanics associated with tibial plateau leveling osteotomy predicted by use of a computer model. *Am J Vet Res*. 2014;75(7):626-632.

57. Kim SE, Pozzi A, Banks SA, Conrad BP, Lewis DD. Effect of Cranial Cruciate Ligament Deficiency, Tibial Plateau Leveling Osteotomy, and Tibial Tuberosity Advancement on Contact Mechanics and Alignment of the Stifle in Flexion. *Vet Surg*. 2010;39(3):363-370.

58. Schultz JA, Allen DA, Bergman PJ. Anatomic femorotibial changes associated with tibial plateau leveling osteotomy. *Can Vet J*. 2015;56:978–982.

59. Larguier L, Hespel A-M, Jamet N, et al. Accuracy and precision of measurements performed on three-dimensional printed pelvises when compared to computed tomography measurements. *J Vet Sci*. 2019;20(3):1-10.

60. Ley B, Daubs B, Bader J, Silverman E. Assessment of the medial collateral ligament as an intra-operative anatomical landmark for tibial plateau levelling osteotomy. *Vet Comp Orthop Traumatol*. 2014;27(04):285-287.
61. Drygas KA, Pozzi A, Goring RL, Horodyski MB, Lewis DD. Effect of Tibial Plateau Leveling Osteotomy on Patellar Tendon Angle: A Radiographic Cadaveric Study. *Vet Surg*. 2010;39(4):418-424.

62. Wilke VL, Zhang S, Evans RB, Conzemius MG, Rothschild MF. Identification of chromosomal regions associated with cranial cruciate ligament rupture in a population of Newfoundlands. *Am J Vet Res*. 2009;70(8):1013-1017.

63. Kim SE, Lewis DD, Pozzi A, Seibert RL, Winter MD. Radiographic quantitative assessment of cranial tibial subluxation before and after tibial plateau leveling osteotomy in dogs. *Am J Vet Res*. 2011;72(3):410-416.

64. Mathis KR, Roe SC, Johnson KA. Tibial Plateau Leveling Osteotomy Plate Contouring and Proximal Load Screw Angulation Affect Osteotomy Compression. *Vet Surg*. 2015;44(8):997-1002.

65. Johnson K, Lanz O, Elder S, McLaughlin R, Were S, Harper T. The effect of stifle angle on cranial tibial translation following tibial plateau leveling osteotomy: An in vitro experimental analysis. *Can Vet J*. 2011;52:961–966.

66. Lackowski WM, Vasilyeva YB, Crooks RM, Kerwin SC, Hulse DA. Microchemical and surface evaluation of canine tibial plateau leveling osteotomy plates. *Am J Vet Res*. 2007;68(8):908-916.

67. Cosenza G, Reif U, Martini FM. Tibial plateau levelling osteotomy in 69 small breed dogs using conically coupled 1.9/2.5 mm locking plates. *Vet Comp Orthop Traumatol*. 2015;28(05):347-354.

68. Lineberger JA, Allen DA, Wilson ER et al. Comparison of radiographic arthritic changes associated with two variations of tibial plateau leveling osteotomy *Vet Comp Orthop Traumatol*. 2005;18(01):13-17.

69. Bernarde A, Diop A, Maurel N, Viguier E. An in vitro biomechanical study of bone plate and interlocking nail in a canine diaphyseal femoral fracture model. *Vet Surg*. 2001;30(5):397-408.